Aerospace Science and Technology 155 (2024) 109364

Contents lists available at ScienceDirect

Aerospace Science and Technology

journal homepage: www.elsevier.com/locate/aescte

Flow dynamics and mixing of jet in crossflow with cylindrical cavity

Bichuan Mo [a], Vigor Yang [a,*], Liwei Zhang [b,*]

[a] School of Aerospace Engineering, Georgia Institute of Technology, Atlanta, GA 30332, USA
[b] Department of Mechanical and Aerospace Engineering, University of Texas at Arlington, Arlington, TX 76019, USA

ARTICLE INFO

Edited by: Dr Mehdi Ghoreyshi

Keywords:
Flow modulation
Mixing enhancement
Jet in crossflow

ABSTRACT

The flow dynamics and mixing characteristics of an air jet issued from a cylindrical cavity in an air crossflow are numerically studied using a large-eddy-simulation technique. The cavity, aligned concentrically with the jet, is located beneath the crossflow wall. The jet-to-crossflow velocity ratio is 4, and the Reynolds number for the jet flow is 1.39×10^4 based on its diameter and centerline velocity. The presence of the cavity significantly influences the early evolution of the jet and its interaction with the crossflow. Complex vortical structures are observed. Notably, windward vortices on the jet surface increase in size, accompanied by a reduction in the Strouhal number. For a deep cavity, these vortices break down and result in small vortical tubes in the jet streamwise direction due to secondary instability. Also examined are leeward shear-layer vortices, hanging vortices, wake vortices, and the recirculating flow within the cavity. Their roles in the mixing between the jet fluid and the crossflow are identified. The cavity enhances mixing. The effect is significant in the near field but diminishes in the far field. By adjusting the cavity radius and depth, it is determined that the cavity depth exercises a more profound impact on jet evolution and mixing than the cavity radius. The most substantial influence occurs when a narrow and deep cavity is implemented. These findings may serve as guidelines for optimizing cavity design for effective modulation of jet behaviors.

1. Introduction

Jet-in-crossflow (JICF) is a common fluid dynamic phenomenon. Extensive studies have been conducted for several decades. Comprehensive reviews of this subject have been provided by Margason [1], Karagozian [2], and Mahesh [3], with surveys of recent advances by Karagozian [4] and Zhang et al. [5,6]. The flow development can be characterized by four major structures [7]: (1) horseshoe vortices originating upstream of the jet, (2) rolling vortices on the windward side of the jet due to Kelvin-Helmholtz instability, (3) a counter-rotating vortex pair (CVP) initiated in the near field, which then develops along the jet trajectory and becomes the dominant structure in the far field, (4) upright vortices in the wake region of the jet due to the vorticity in the crossflow wall boundary layer [7–10]. Among these structures, the CVP plays a vital role in determining the mixing characteristics of the jet with the surrounding fluid [2,11].

Flow dynamics and mixing characteristics are major concerns for a JCIF system, especially for engineering applications. For example, in many chemical-energy conversion devices, fuel is transversely injected to mix with oxidizer in the crossflow. A small variation in mixedness can lead to unexpected hazardous outcomes [12,13]. Considerable effort has been expended to study this subject, and a comprehensive understanding has been established [11,14–19]. Smith and Mungal [14] investigated issues related to mixing, structure, and scaling. It was concluded that far-field mixing is mainly attributed to the CVP, while near-field mixing is associated with the structural formation of the CVP. They developed three scaling laws for the vortex interaction region: the jet trajectory, the decay rate of the centerline jet-fluid concentration, and the separation between the near and far fields. Su and Mungal [15] conducted simultaneous measurements of the jet-fluid concentration and velocity fields with a jet-to-crossflow velocity ratio $R = 5.7$ and a jet Reynolds number Re_j about 5000. Results suggested jet-like and wake-like scaling for the velocity field in the near and far fields, respectively. The disparity of the scaling properties between the jet-fluid concentration and the velocity fields was noted. Muppidi and Mahesh [9,16,20] examined jet-fluid mixing properties using direct numerical simulations under flow conditions corresponding to the experiment by Su and Mungal [15]. The downstream side of the jet was found to contribute significantly to crossflow entrainment. The high entrainment rate of the jet was attributed to the high pressure at the saddle node

* Corresponding authors.
E-mail addresses: vigor.yang@aerospace.gatech.edu (V. Yang), liwei.zhang@uta.edu (L. Zhang).

https://doi.org/10.1016/j.ast.2024.109364
Received 1 March 2024; Received in revised form 29 June 2024; Accepted 29 June 2024
Available online 1 July 2024
1270-9638/

caused by the impinging crossflow in the symmetric plane, which drives the crossflow toward the jet.

Shan and Dimotakis [17] showed that the probability density function of jet-fluid concentration evolves from a monotonically decreasing function to a strongly peaked function with increasing Re_j, and anisotropy exists at the smallest scales of the jet-fluid concentration field. Shear layer instability was found to have a major influence on jet mixing behaviors. Megerian et al. [21] examined the dominant frequencies of shear layer instability at different Re_j. The response to low-level forcing was examined over a wide range of jet-to-crossflow velocity ratios, with special attention given to the transition from absolute to convective instability. Mahesh and colleagues [22–24] studied situations with $Re_j = 2000$ and $R = 2$, 4 under the same conditions considered by Megerian et al. [21] The shear layer is most sensitive to perturbations along the upstream side of the jet, while in the downstream region, the wall boundary layer plays a more important role in affecting the low-frequency modes of jet instability. Shoji et al. [25] further examined the analogy between the upstream shear layer immediately after jet injection and a local counter-current shear layer, as proposed by Iyer and Mahesh [22], to study the origin of shear layer transition along the jet. All of the above studies were limited to jets with low speed and low Re. Zhang et al. [5,6] considered flow conditions of practical gas-turbine operation, including the jet centerline velocity $U_j = 160\ m/s$, crossflow velocities $U_\infty = 40$ and 80 m/s, and jet Reynolds number $Re_j = 1.3 \times 10^4$. Both stationary and oscillating crossflow conditions were studied. The jet flow dynamics and mixing characteristics in response to flow oscillations arising from the downstream region were explored systematically.

In addition to the canonical study of JICF, efforts have been made to investigate jet flow and mixing behaviors with different injection orifice geometries [26,27] and injection angles [28], as well as the use of vortex generators [29] and active control [2,4,30]. Geometrical modification of the injection configuration is of particular relevance here. Haven and Kurosaka [26] observed the formation of double-deck kidney and anti-kidney vortices from rectangular and elliptic injection orifices. New et al. [27] examined the situations involving elliptic jets. For a jet with a low aspect ratio, two adjacent CVPs form initially, and the weaker CVP is subsequently entrained by the stronger CVP in the downstream. For a high aspect-ratio jet, a windward vortex pair develops due to the additional folding of the shear layer on the windward side of the jet. The effect of aspect ratio is significant only in the near field and diminishes in the far field. The process leading to the formation of large-scale jet structures (i.e., leading-edge and lee-side vortices) is similar across different elliptic shapes to that of a circular jet [31]. Harris et al. [32] and Morse and Mahesh [33] studied, both experimentally and numerically, the effects of tabs on shear layer instability, vortex structure, and mixing. An upstream placement of a tab, compared to other locations, has a more profound effect in weakening the upstream shear-layer instability, altering the cross-section structures, and enhancing mixing. It is worth noting that the Reynolds number and velocities of the jet and the crossflow in these studies are typically low. Their application to practical engineering systems remains to be clarified.

As discussed by Zhang et al. [5,6], the dynamics of jet flow and its mixing characteristics are influenced by crossflow conditions. In addition to the injection geometry, it is crucial to configure the environment into which the injection is introduced. This effect is particularly important when complex geometries, such as cavities, are involved in the JICF applications in practical systems. Extensive efforts have been expended to study flows over cavities [34–38] and backward-facing steps [39]. Crook et al. [34] examined the effects of cavity length l and depth h. Two distinct flow regimes were identified: one with a large recirculation zone in the cavity and a shear layer bridging the entire cavity for $l/h \leq 6 \sim 7$, known as the "open-type"; and the other with two vortices attached to the front and back ends of the cavity, with no center recirculation zone for $l/h \geq 8 \sim 9$, known as the "closed-type".

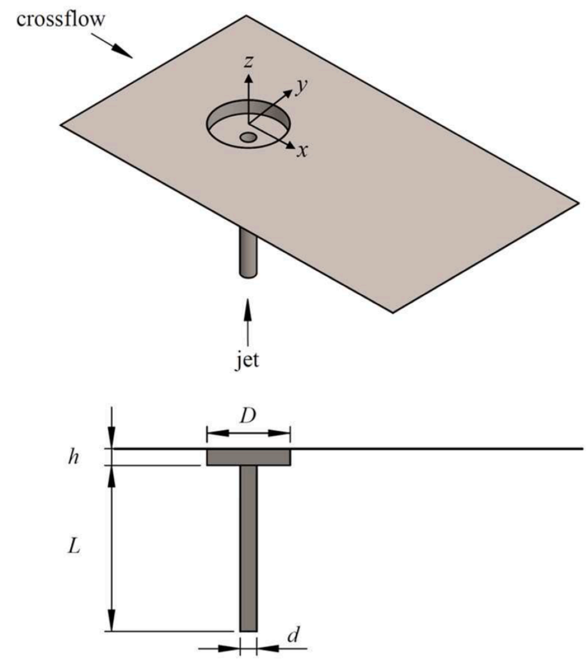

Fig. 1. Schematic of the JICF system with a cylindrical cavity. D and h represent the diameter and depth of the cavity, respectively, while d and L denote the diameter and length of the injection tube, respectively.

Rowley et al. [35] studied self-sustained oscillations in two-dimensional flows over rectangular cavities. Larchevêque et al. [36–38] conducted large-eddy simulations to explore three-dimensional cavity flow characteristics and their asymmetric effects. Le et al. [39] investigated the flow over a backward-facing step with an expansion ratio of 1.2 and $Re = 5100$ using direct numerical simulation.

The present work explores the flow dynamics and mixing characteristics of the JICF with a cylindrical cavity surrounding the concentric injection orifice, as shown schematically in Fig. 1. The cavity is utilized to generate vortices, modulating the initial evolution of the jet and the subsequent flow development. Four different cavity geometries are studied. Special attention is given to the cavity flow structure, the windward rolling vortices of the jet, their interaction with the crossflow, and the jet mixing characteristics. The paper is organized as follows. Section 2 describes the theoretical formulation and numerical framework. Section 3 discusses the computational domain and boundary conditions. Section 4 presents both the instantaneous and time-averaged flowfields for different cavity geometries. Section 5 provides the statistical results of the mixing characteristics. Section 6 concludes the study and offers suggestions for applications.

2. Theoretical formulation and numerical framework

The theoretical formulation is based on the conservation equations of mass, momentum, energy, and species concentration in three dimensions. It is well documented in Refs. [5,40,41]. The present analysis employes a large-eddy simulation (LES) technique for turbulence closure, wherein large-scale eddies are resolved, and small subgrid-scale (sgs) motions are modeled. The Favre-filtered conservation equations can be written as:

$$\text{mass} \quad \frac{\partial \overline{\rho}}{\partial \mathrm{t}} + \frac{\partial \overline{\rho} \widetilde{\mathrm{u}}_\mathrm{j}}{\partial \mathrm{x}_\mathrm{j}} = 0 \tag{1}$$

$$\text{momentum} \quad \frac{\partial \overline{\rho} \widetilde{\mathrm{u}}_\mathrm{i}}{\partial \mathrm{t}} + \frac{\partial \left(\overline{\rho} \widetilde{\mathrm{u}}_\mathrm{i} \widetilde{\mathrm{u}}_\mathrm{j} + \overline{p} \delta_{\mathrm{ij}} \right)}{\partial \mathrm{x}_\mathrm{j}} = \frac{\partial \left(\widetilde{\tau}_{\mathrm{ij}} - \tau_{\mathrm{ij}}^{\mathrm{sgs}} \right)}{\partial \mathrm{x}_\mathrm{j}} \tag{2}$$

energy $$\frac{\partial\overline{\rho}\widetilde{E}}{\partial t}+\frac{\partial((\overline{\rho}\widetilde{E}+\overline{p})\widetilde{u}_i)}{\partial x_i}=\frac{\partial}{\partial x_i}\left(\widetilde{u}_j\widetilde{\tau}_{ij}+\lambda\frac{\partial\widetilde{T}}{\partial x_i}-H_i^{sgs}+\sigma_i^{sgs}\right) \tag{3}$$

species concentration $$\frac{\partial\overline{\rho}\widetilde{Y}_k}{\partial t}+\frac{\partial(\overline{\rho}\widetilde{u}_j\widetilde{Y}_k)}{\partial x_j}=\frac{\partial}{\partial x_j}\left(-\overline{\rho}\widetilde{Y}_k\widetilde{U}_{k,j}-\Phi_{k,j}^{sgs}-\Theta_{k,j}^{sgs}\right) \tag{4}$$

where overbar denotes the spatial-filtering operation and tilde the Favre-filtering operation, i.e. $\widetilde{f}=\overline{\rho f}/\overline{\rho}$. The variables $\rho, u_i, p, E, T, \tau_{ij}$, Y_k, and $U_{k,j}$ represent the density, velocity, pressure, total specific energy, temperature, viscous stress, mass fraction and diffusion velocity of species, respectively. Fick's law is used to evaluate the diffusive flux. The ideal gas equation of state is used. The sgs terms are:

$$\tau_{ij}^{sgs}=\left(\overline{\rho u_i u_j}-\overline{\rho}\widetilde{u}_i\widetilde{u}_j\right) \tag{5}$$

$$H_i^{sgs}=\left(\overline{\rho E u_i}-\overline{\rho}\widetilde{E}\widetilde{u}_i\right)+\left(\overline{pu_i}-\overline{p}\widetilde{u}_i\right) \tag{6}$$

$$\sigma_i^{sgs}=\left(\overline{u_j\tau_{ij}}-\widetilde{u}_j\widetilde{\tau}_{ij}\right) \tag{7}$$

$$\Phi_{k,j}^{sgs}=\left(\overline{\rho Y_k u_j}-\overline{\rho}\widetilde{Y}_k\widetilde{u}_j\right) \tag{8}$$

$$\Theta_{k,j}^{sgs}=\left(\overline{\rho Y_k U_{k,j}}-\overline{\rho}\widetilde{Y}_k\widetilde{U}_{k,j}\right) \tag{9}$$

They are treated using the compressible-flow version of the Smagorinsky model proposed by Erlebacher et al. [42] due to its reasonable accuracy and simplicity. The anisotropic part of the sgs stress is treated using the Smagorinsky model and the isotropic part, τ_{kk}^{sgs}, is modelled with the formulation proposed by Yoshizawa [43],

$$\tau_{ij}^{sgs}-\frac{1}{3}\delta_{ij}\tau_{kk}^{sgs}=-2\nu_t\overline{\rho}\left(\widetilde{S}_{ij}-\frac{1}{3}\widetilde{S}_{kk}\delta_{ij}\right) \tag{10}$$

$$\tau_{kk}^{sgs}=2\overline{\rho}k^{sgs}=2C_I\overline{\rho}(D\Delta)^2|\widetilde{S}|^2 \tag{11}$$

where $\nu_t=C_R(D\Delta)^2|\widetilde{S}|$, $\widetilde{S}_{ij}=\frac{1}{2}\left(\frac{\partial\widetilde{u}_j}{\partial x_i}+\frac{\partial\widetilde{u}_i}{\partial x_j}\right)$, $k^{sgs}=\frac{1}{2}(\widetilde{u_iu_i}-\widetilde{u}_i\widetilde{u}_i)$.

The dimensionless parameters $C_R=0.012$ and $C_I=0.0066$ are obtained from the Yoshizawa [43] model for weakly compressible turbulent flows. The van Driest damping function is used to model the near-wall effect [44],

$$D=1-\exp\left(1-(y^+)^3\Big/25^3\right) \tag{12}$$

where $y^+=yu_\tau/\nu$ and u_τ is the friction velocity.

The sgs energy flux H_j^{sgs} is modelled as

$$H_j^{sgs}=-\overline{\rho}\frac{\nu_t}{Pr_t}\left(\frac{\partial\widetilde{h}}{\partial x_j}+\widetilde{u}_i\frac{\partial\widetilde{u}_i}{\partial x_j}+\frac{1}{2}\frac{\partial k^{sgs}}{\partial x_j}\right) \tag{13}$$

where Pr_t represents the turbulent Prandtl number and a standard value of 0.7 is used here.

The convective species flux term is approximated as

$$\Phi_{k,i}^{sgs}=-\overline{\rho}\frac{\nu_t}{Sc_t}\frac{\partial\widetilde{Y}_k}{\partial x_i} \tag{14}$$

where Sc_t is the turbulent Schmidt number and a value of 0.9 is used in this work.

The sgs viscous diffusion term, σ_{ij}^{sgs}, is neglected due to small contribution to the total energy equation. The sgs species diffusive flux $\Theta_{k,j}^{sgs}$, which comes from the correlation between species mass fraction with diffusive velocity, is also ignored. The use of the static Smagorinsky model in the present study is justified in Refs. [5,40,41].

The numerical framework employs a density-based, finite-volume methodology [40,41]. Temporal integration is achieved using a fourth-order Runge-Kutta method with explicit physical time stepping. Spatial discretization is performed using a second-order central difference scheme in a generalized coordinate. Fourth-order scalar artificial dissipation is implemented. Finally, a multi-block domain decomposition along with a message passing interface is applied to optimize computational efficiency.

3. Computational domain and flow conditions

Fig. 1 shows schematically the JICF configuration, featuring a cylindrical cavity concentric to the jet. The jet has a diameter of $d=1.27\ mm$. The computational domain above the cavity spans a rectangular region defined by the dimensions $-8\le x/d\le 20$, $-8\le y/d\le 8$, and $0\le z/d\le 15$ in the streamwise, spanwise and transverse directions, respectively. The flow evolution within the injection pipe, with a length of $L=10d$, is considered. The coordinate origin is located at the center of the cavity on the crossflow surface.

Air at 1 atm and 300 K is selected as the working fluid for both the jet and the crossflow. To investigate the mixing process, air originating from the injection orifice and from the upstream boundary of the crossflow is treated as two distinct species. The corresponding species equations are solved separately. The velocities of the jet and the crossflow are chosen to be $U_j=160\ m/s$ and $U_\infty=40\ m/s$, respectively, to simulate the flow conditions of operational gas turbine engines. The jet-to-crossflow velocity ratio is $R=U_j/U_\infty=4$, and the corresponding momentum flux ratio is $J=\rho_jU_j^2/\rho_\infty U_\infty^2=16$. Table 1 summarizes the cavity geometries parameterized by the radius r and depth h, along with the total number of numerical cells employed for each case in this study. The mean velocity profile at the entrance of the injection pipe follows that of a developed turbulent pipe flow [45]. Broad-band noise with an intensity of 1% of the mean velocity is imposed at the entrance. A uniform inflow condition is implemented at the inlet of the crossflow domain. The turbulent Prandtl and Schmidt numbers are set to 0.7 and 0.9, respectively.

The numerical grid sizes near the surface of the injection pipe and the cavity wall are $0.0085d$ and $0.01d$, respectively; the corresponding cell-center locations in the wall units are $r_j^+=2.76$ and $r^+=3.25$, respectively. The largest grid sizes in the cavity in the radial and transverse directions are both set to be $0.015d$. In the circumferential direction, the largest grid sizes are $0.0227d$ for Cases 1 and 3, and $0.0378d$ for Cases 2 and 4, respectively. In the transverse direction of the crossflow, the grid is refined near the wall $0\le z/d\le 3$ with a minimum grid size of $z^+=3.25$. It remains fixed at $0.05d$ for $3\le z/d\le 13$, and then linearly increases to $0.186d$ at the boundary of the computational domain at $z/d=15$. In the streamwise and spanwise directions, the grid size ranges from $0.025d$ to $0.056d$. Overall, the average grid size across all cases is approximately $0.038d$. The Reynolds number, based on the jet diameter and the centerline velocity at the injection orifice, is $Re_j=U_jd/\nu=1.39\times 10^4$. The corresponding Kolmogorov scale η and Taylor microscale λ are, respectively,

$$\eta=Re_j^{-3/4}\cdot d=0.00078d \tag{15}$$

$$\lambda=Re_j^{-1/2}\cdot d=0.0085d \tag{16}$$

Table 1
Cavity geometries and number of numerical cells.

Cases	Cavity radius r/d	Cavity depth h/d	Total number of cells ($\times 10^6$)
Baseline	N/A	N/A	110.9
1	1.5	0.5	115.9
2	1.5	1.0	117.7
3	2.5	0.5	123.8
4	2.5	1.0	126.5

The average grid size is comparable to the Taylor microscale, making it suitable for the current LES study. The near-wall resolutions, r_j^+, r^+ and z^+, are approximately 3, allowing for adequate treatment of the boundary layers.

At the inflow boundary, the jet and crossflow velocities are set to the aforementioned values. Pressure is extrapolated from interior points, and temperature is calculated using the isentropic relationship with pressure. The outflow boundary condition is determined by extrapolating the primitive variables. No-slip, isobaric, and adiabatic boundary conditions are enforced on the walls. The simulation is initialized with a jet velocity of 20 m/s and a crossflow velocity of 5 m/s, which then linearly ramp up over time to the specified flow conditions. The timestep is set at 2×10^{-9} s, and the corresponding Courant-Friedrichs-Lewy (CFL) number is approximately 0.2, based on the local velocity and grid size. Data acquisition begins after one flow-through time to allow the crossflow to flush the entire computational domain. The recording period lasts for three flow-through times to acquire sufficient snapshots and statistics.

In our previous studies of transverse jets in both stationary and oscillating crossflows [5,6], the overall approach was validated against

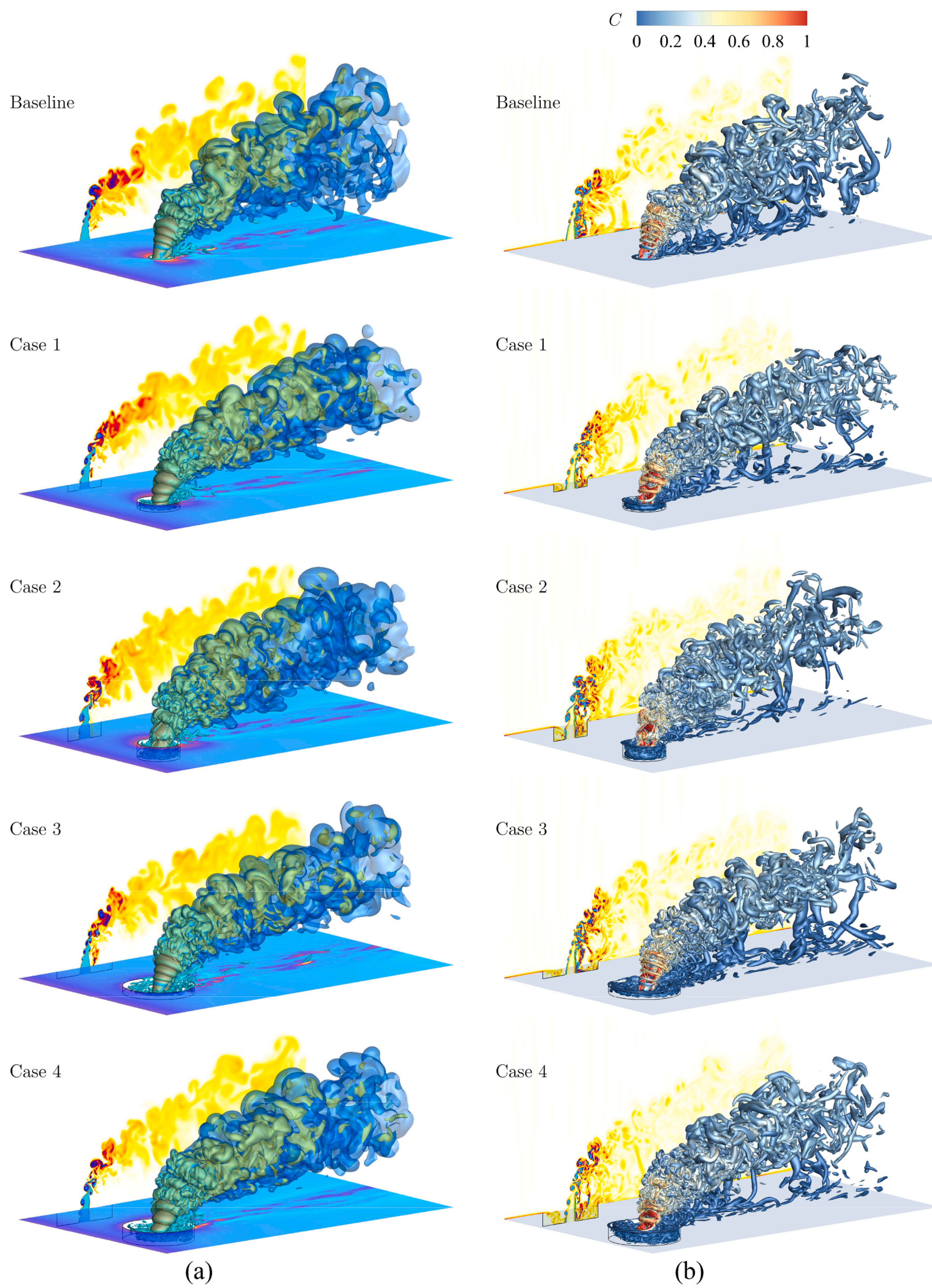

Fig. 2. Snapshots of (a) isosurfaces of $C = 0.9,\ 0.2,\ 0.05$ (colored red, yellow, blue, respectively) and $Q = 1 \times 10^{10} s^{-2}$ (cyan); the back panel shows the jet-fluid concentration C on the $y = 0$ plane, while the bottom panel shows the shear stress on the $z = 0$ plane; and (b) isosurfaces of $Q = 5 \times 10^{8} s^{-2}$ (colored by C) and isosurfaces of $|V| = 4m/s$ (colored blue); the back panel shows the vorticity magnitude on the $y = 0$ plane.

the experimental findings reported by Su and Mungal [15]. Additionally, a comprehensive grid independence study was conducted for the baseline case as detailed in Ref. [5]. The study employed three grid resolutions with average grid sizes of 0.047d, 0.071d, and 0.12d, each of which is larger than the average grid size of 0.038d in the present study. For the sake of brevity, the verification and validation processes are not included in the current paper.

4. Flow dynamics

After the initial numerical transient phase, the instantaneous results for each case are closely examined. Fig. 2 shows snapshots of the flow structures associated with different cavity configurations. The baseline case without a cavity is also included. Vortical structures are identified using the Q-criterion [46,47], defined as the second invariant of the velocity gradient tensor,

$$Q = \frac{1}{2}\left(||\Omega||^2 - ||S||^2\right) = -\frac{1}{2}(\lambda_1 + \lambda_2 + \lambda_3) \tag{17}$$

where S and Ω are the symmetric and antisymmetric components of the velocity gradient tensor, respectively, with $\lambda_1 \geq \lambda_2 \geq \lambda_3$ being the eigenvalues of $S^2 + \Omega^2$. For cases where the velocity divergence is negligible, this Q-criterion is simplified as [47]:

$$Q = -\frac{1}{2}\left(\left(\frac{\partial u}{\partial x}\right)^2 + \left(\frac{\partial v}{\partial y}\right)^2 + \left(\frac{\partial w}{\partial z}\right)^2 + 2\frac{\partial u}{\partial y}\frac{\partial v}{\partial x} + 2\frac{\partial u}{\partial z}\frac{\partial w}{\partial x} + 2\frac{\partial v}{\partial z}\frac{\partial w}{\partial y}\right) \tag{18}$$

The Q-criterion delineates the balance between the shear strain rate and vorticity magnitude [46]. In the current study, the Q-criterion is normalized by $(U_j/d)^2$, where U_j is the jet centerline velocity and d the jet diameter.

In Fig. 2a, the isosurfaces of $Q = 1 \times 10^{10} s^{-2}$ (colored cyan) are presented, along with isosurfaces of the jet-fluid concentration at $C =$ 0.9, 0.2, 0.05 (colored red, yellow, blue, respectively). The normalized Q-value is $Q/(U_j/d)^2 = 0.63$. The cavity exerts a strong influence on the near-field behaviors of the jet, leading to larger windward rolling vortices with reduced characteristic frequencies compared to the baseline case without a cavity. These vortices subsequently break down and deform while traveling downstream, due to intensive interactions between the jet and cavity flow. This effect is more pronounced in cases with deeper cavities (i.e., Cases 2 and 4). The back panel reveals the jet-fluid concentration C on the $y = 0$ plane, revealing the jet vortex structures. The bottom panel shows the shear stress on the $z = 0$ surface, indicating a shift in the high shear region from the lateral sides of the jet to the windward or leeward sides of the cavity. A change in the wake vortex pattern is also observed.

Fig. 2b shows the isosurfaces of $Q = 5 \times 10^8 s^{-2}$ (normalized value of 0.0315 and colored by the jet-fluid concentration C), and the isosurfaces of the velocity magnitude $|V| = 4\ m/s$ (colored blue). The back panel displays the vorticity magnitude on the $y = 0$ plane, highlighting the vortical structures in the initial stage of jet development. At this low Q-value, the fingerlike, roller-structured wake vortices are distinctly visible, linking the near-wall region with the jet plume. These structures play a crucial role in crossflow entrainment, as evidenced by the absence of jet fluid within these vertical rollers. In the absence of a cavity, wake vortices, originating from the crossflow boundary layer upstream of the jet injection orifice, form when the boundary layer separates upon sweeping around the jet in the early wake region and encountering an adverse pressure gradient on the jet leeward side [7]. The presence of a cavity enhances the crossflow boundary-layer separation and strengthens wake vortices. The phenomenon becomes more obvious in Cases 3 and 4 with wider cavities. Another notable feature is the vortical structures inside the cavity, also shown by a higher Q-value in Fig. 2a. Robust vortices encircle the nascent jet from the injection orifice and exert significant influence on the jet evolution. These vortices exhibit a strong dependency on the cavity depth, as evidenced in Cases 2 and 4, which have deeper cavities.

To investigate the effect of cavity on jet mixing, Fig. 3 shows snapshots of near-field flow structures using the isosurface of $Q = 1 \times 10^{11}\ s^{-2}$ (normalized value of 6.3), colored by jet fluid concentration C. Stronger values than those in Fig. 2 are used to emphasize the near-field structures. Close to the jet exit, spanwise rollers sequentially appear on the windward side of the jet plume, showcasing the shear-layer vortices in the initial jet region induced by the Kelvin–Helmholtz instability. As the jet penetrates deeper into the crossflow, the shear layer destabilizes and rolls up into small vortices. These structures are subsequently advected downstream and further amplified by the entraining crossflow, creating a wavy upper boundary of the jet plume. The influence of the cavity on the jet flow dynamics manifests in several aspects. First, the presence of the cavity increases the size of the windward rolling vortices along the jet surface, indicative of enhanced vortex strength, while showing a reduced characteristic frequency. In Case 2, windward rolling vortices break down and result in small vortical tubes in the jet streamwise direction due to secondary instability. Second, in the absence of a cavity, the shear layer on the leeward side of the jet encounters a weak adverse pressure gradient and limited crossflow entrainment, resulting in fewer roll-up vortices. With a cavity, however, the pressure distribution near the injection orifice and the local pressure gradients are changed, leading to more pronounced rolling vortices, particularly in Cases 2 and 4 with deeper cavities. Third, without a cavity, the crossflow deflects around the jet and accelerates on the lateral sides, which induces a skewed mixing layer and promotes hanging vortices in the direction of the mean convective velocity. These vortices transport the jet fluid towards the lower half of the jet plume while increasing its horizontal momentum. The presence of a cavity significantly amplifies this flow behavior, as evidenced by increased hanging vortices, especially in Cases 2 and 4. Lastly, as the jet moves downstream, the rolling vortices lose their regularity and gradually disintegrate. This transition occurs over the shortest distance in Case 2 with a narrow and deep cavity.

The near-field flow structures are further explored using time-averaged results. Fig. 4a shows the isosurfaces of $\langle Q \rangle = 1 \times 10^9 s^{-2}$ (normalized value of 0.063) calculated from the time-averaged velocity field. They are colored by the time-averaged jet-fluid concentration $\langle C \rangle$. In Case 1, which has a narrow and shallow cavity, a well-structured vortex ring occupies the cavity. As the cavity depth increases in Case 2, the vortex ring in the cavity increases in size; meanwhile, the isosurfaces exhibit discontinuity and begin to decay on the windward and leeward sides of the jet. Cases 3 and 4, both with wider cavities, present similar flowfields. Nonetheless, the vortex ring structure appears disrupted and further detached from the jet, a phenomenon attributed to the reduced flow confinement due to an increased cavity radius. Cases 2 and 4 have deeper cavities and exhibit lower jet-fluid concentrations compared to Cases 1 and 3, suggesting that an increase in cavity depth enhances near-field mixing. Case 2 features a narrow cavity. The maximum jet-fluid concentration has its smallest value among all cases. A smaller cavity radius benefits near-field mixing.

Fig. 4b shows the isosurfaces of time-averaged jet-fluid concentration at $\langle C \rangle = 0.9$, 0.2, and 0.05 (colored red, yellow, and blue, respectively). Also shown are the isosurfaces of $\langle Q \rangle = 1 \times 10^{10} s^{-2}$ (normalized value of 0.63, and colored cyan) based on the time-averaged velocity field. The back panel shows the distribution of jet-fluid concentration C on the $y = 0$ plane, while the bottom panel reveals the shear-stress field on the crossflow wall at $z = 0$. As evidenced by the isosurface of $\langle C \rangle = 0.2$, the jet gradually bends upon encountering the crossflow in the baseline case without a cavity. This behavior, however, alters with the presence of a cavity. As the cavity depth increases, the jet trajectory initially remains relatively straight after leaving the injection orifice and then bends more significantly upon

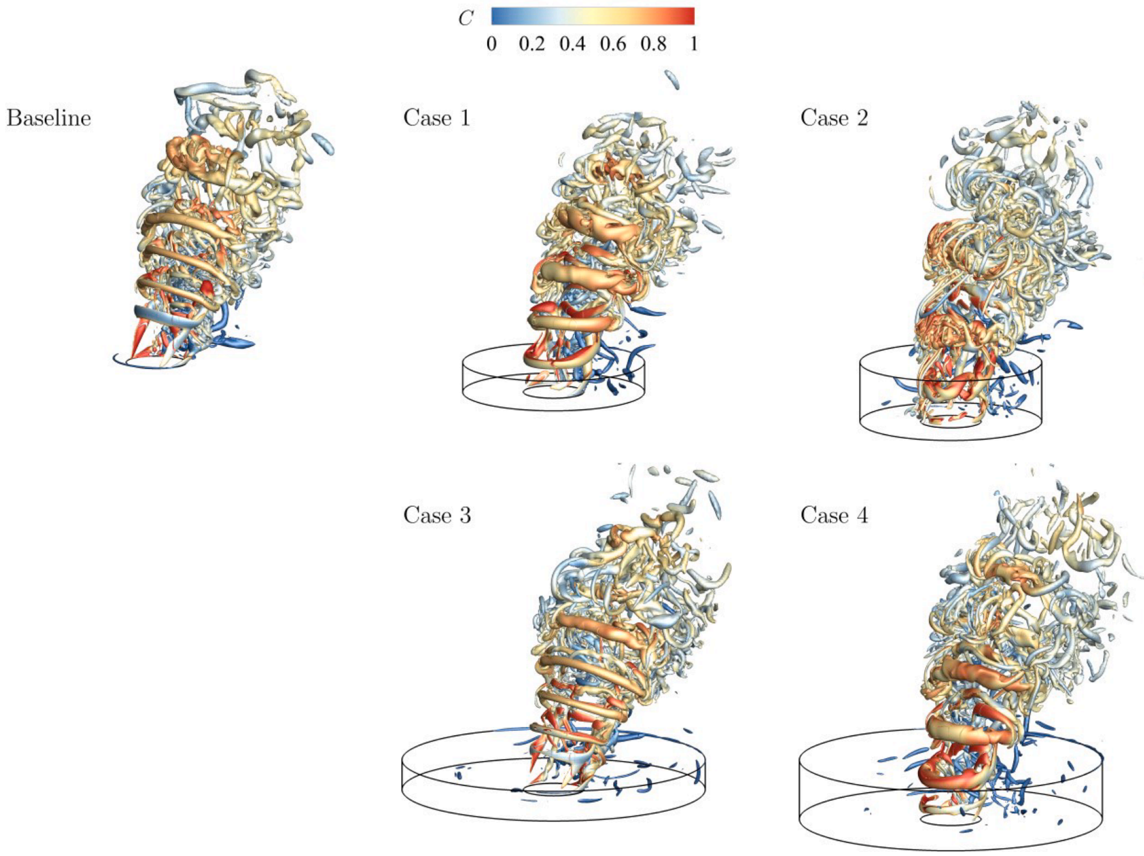

Fig. 3. Snapshots of near-field flow structures: isosurface of $Q = 1 \times 10^{11} s^{-2}$ (colored by C).

interacting with the crossflow. Such behavior is further revealed on the $y = 0$ plane, where the jet-fluid concentration field is displayed. In Cases 1 and 2 (smaller cavity radius), the high-shear stress region shifts from the lateral sides of the jet to the front and lateral edges of the cavity. In Cases 3 and 4 (larger cavity radius), it shifts to the leeward side of the jet. In addition, a notable decrease in the maximum shear stress is observed across these cases.

The vortical flow structure of the jet fluid is further explored. Lasheras and Choi [48] experimentally studied the vortical field of a planar free shear layer. Streamwise vortices are formed due to the stretching of vorticity on the braids in the principal direction of the positive strain field created by the spanwise vortices. Morse and Mahesh [33] investigated the shear-layer dynamics of a tab JICF system by means of direct numerical simulation. It was found that streamwise vortices curl around spanwise vortex tubes when the tab is located upstream of the injection orifice. A similarity between the streamwise vortices and the strained oriented vortex tubes observed in [48] is noticed. Ruiz et al. [47] studied the JICF flow topology using LES. The azimuthal instability of ring vortices was shown to lead to the formation of v-shape vortices.

The formation mechanism of the streamwise vortex tubes along the jet can be identified using the vorticity transport equation [49], as shown below.

$$\frac{D\omega}{Dt} = (\omega\cdot\nabla)u - \omega(\nabla\cdot u) + \frac{1}{\rho^2}\nabla\rho\times\nabla p + \nabla\times\left(\frac{\nabla\times\tau}{\rho}\right) \tag{19}$$

where ω, u and τ are the vorticity vector, velocity vector and viscous stress tensor, respectively. Those terms on the right-hand side represent the effects of vortex stretching/tilting, volume dilatation, baroclinic torque, and viscous diffusion, respectively. The vortex stretching/tilting term contains contributions from stretching and tilting [33]:

$$(\boldsymbol{\omega}\cdot\nabla)\boldsymbol{u} = (\boldsymbol{\omega}\cdot\boldsymbol{S}\cdot\boldsymbol{e}_\omega)\boldsymbol{e}_\omega + (\boldsymbol{\omega}\cdot\boldsymbol{S}\cdot\boldsymbol{e}_t)\boldsymbol{e}_t \tag{20}$$

where $\boldsymbol{S}$ is the strain-rate tensor, $\boldsymbol{e}_\omega$ a unit vector of vorticity, $\boldsymbol{e}_\omega = \boldsymbol{\omega}/|\boldsymbol{\omega}|$, and $\boldsymbol{e}_t$ a unit vector perpendicular to the vorticity vector, $\boldsymbol{e}_t = (\boldsymbol{\omega}\cdot\boldsymbol{S} - (\boldsymbol{\omega}\cdot\boldsymbol{S}\cdot\boldsymbol{e}_\omega)\boldsymbol{e}_\omega)/|\boldsymbol{\omega}\cdot\boldsymbol{S} - (\boldsymbol{\omega}\cdot\boldsymbol{S}\cdot\boldsymbol{e}_\omega)\boldsymbol{e}_\omega|$. Here the magnitudes of vortex stretching $\boldsymbol{\omega}\cdot\boldsymbol{S}\cdot\boldsymbol{e}_\omega$ and vortex tilting $\boldsymbol{\omega}\cdot\boldsymbol{S}\cdot\boldsymbol{e}_t$ are denoted as V_s and V_t, respectively.

For illustration, Fig. 5 shows the near-field vortical structures of Case 2, presented by the iso-surfaces of (a) $Q = 1 \times 10^{11}\ s^{-2}$, colored by jet fluid concentration C, and z vorticities $\omega_z = -1 \times 10^6\ s^{-1}$ (blue) and $1 \times 10^6\ s^{-1}$ (red) (normalized values $\omega_z/(U_j/d) = \pm 7.94$), (b) $Q = 1 \times 10^{11}\ s^{-2}$ and vortex stretching magnitudes $V_s = -3 \times 10^{11}\ s^{-2}$ (blue) and $3 \times 10^{11}\ s^{-2}$ (red) (normalized value $V_s/(U_j/d)^2 = \pm 18.9$), and (c) $Q = 1 \times 10^{11}\ s^{-2}$ and vortex tilting magnitude $V_t = 3 \times 10^{11}\ s^{-2}$ (cyan, and normalized value $V_t/(U_j/d)^2 = 18.9$). As an example, attention is given to the streamwise vortex tube in the dotted box in Fig. 5a. When stretching downward, the z-vorticity component ω_z has a negative value on the left side of the vortex tube and a positive value on the right side. When 'restoring' in the spanwise direction, the vortex tube remains aligned with the windward rolling vortices. This suggests that the streamwise vortex tube is formed due to the stretching and displacement of the original weak vortex filament by the strong windward rolling vortices, instead of the shearing of the jet in the azimuthal direction caused by the Kelvin-Helmholtz instability, which otherwise would lead to the same sign of the z-vorticity on either the left or right side of the vortex tube. In Fig. 5b, the isosurface of vortex stretching magnitude $V_s = 3 \times 10^{11} s^{-2}$ (red) confirms that the streamwise vortex tube undergoes stretching. A large part of the windward rolling vortices also undergoes stretching. The isosurface of the vortex stretching magnitude $V_s = -3 \times 10^{11} s^{-2}$ (blue) indicates that vortex

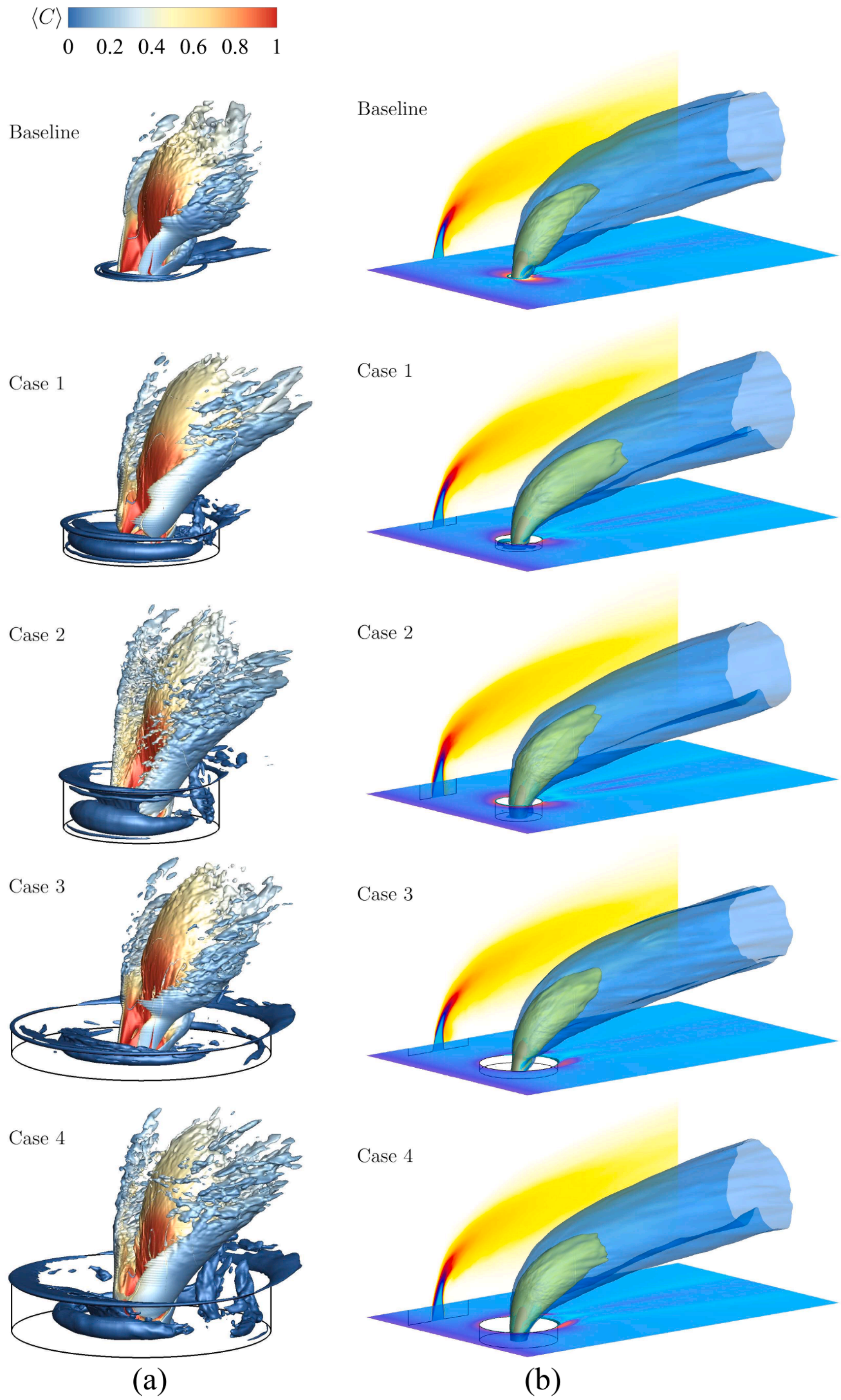

Fig. 4. Time-averaged flowfield: (a) isosurfaces of $\langle Q\rangle = 1\times10^{9}s^{-2}$ (colored by $\langle C\rangle$); and (b) isosurfaces of $\langle C\rangle = 0.9,\ 0.2,\ 0.05$ (colored red, yellow, blue) and $\langle Q\rangle = 1\times10^{10}s^{-2}$ (colored cyan); the back panel shows $\langle C\rangle$ on the $y = 0$ plane; and the bottom panel shows the shear stress on the $z = 0$ plane.

contraction mainly occurs in the bottom part of the streamwise vortex tube where the breakdown of windward rolling vortices take place. The near-field structure suggests the prevalence of stretching over contraction. Fig. 5c indicates that vortex tilting is associated with windward rolling vortices and streamwise vortex tubes. The near-field jet flow structure is mainly dictated by the states of vortex stretching, contraction and tilting.

The mechanisms of windward rolling vortex breakdown and streamwise vortex tube formation along the jet are summarized as follows. The coupling between the cavity recirculating flow and the jet creates strong shearing on the windward side of the jet. The helical motion of the cavity flow surrounding the jet provides additional stress. Combined, windward rolling vortices distort or even break down due to vortex stretching and tilting. In the meantime, streamwise vortex tubes are formed by secondary instability. The strong windward rolling vortices create a strain field for the weak vortex filaments which have the same vorticity direction as those of windward rolling vortices. The principal direction of the positive strain field is along two consecutive windward rolling vortices. The vortex filament undergoes stretching in the principal direction of the strain field [48], along with some tilting, to form a streamwise vortex tube. The flow unsteadiness in the cavity further contributes to the stretching, tilting and displacing of vortex

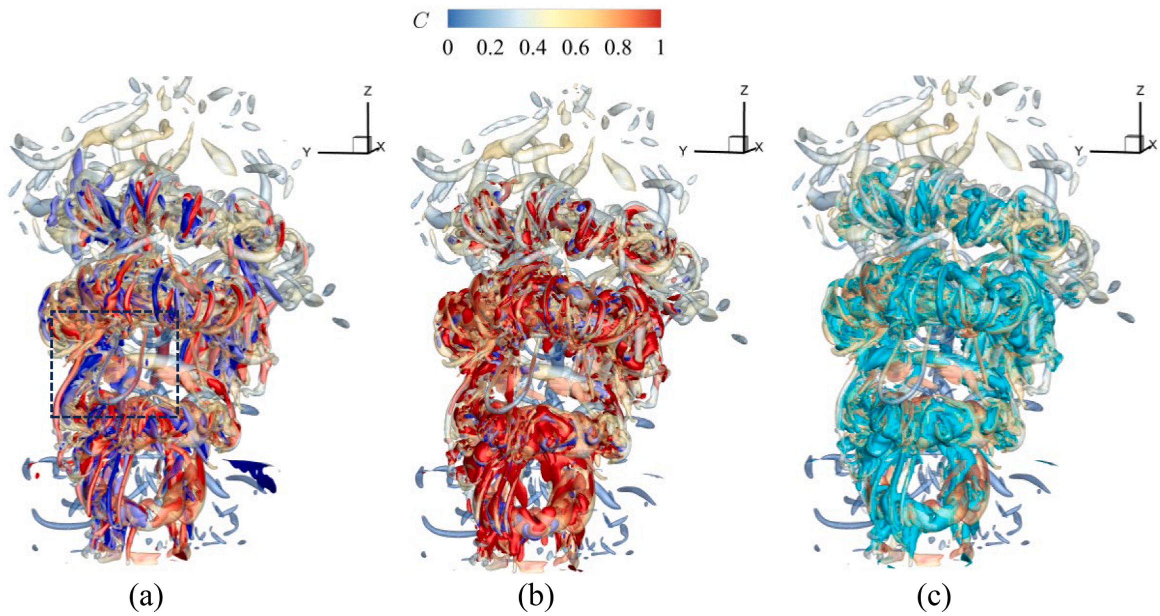

Fig. 5. Near-field vortical structures of Case 2. Iso-surfaces of (a) $Q = 1 \times 10^{11} s^{-2}$ (colored by C), and z vorticity $\omega_z = -1 \times 10^6\ s^{-1}$ (blue) and $\omega_z = 1\ \times 10^6\ s^{-1}$ (red), (b) $Q = 1 \times 10^{11} s^{-2}$ (colored by C), and vortex stretching magnitudes $V_s = -3 \times 10^{11}\ s^{-2}$ (blue) and $3 \times 10^{11}\ s^{-2}$ (red), and (c) $Q = 1 \times 10^{11} s^{-2}$ (colored by C), and vortex tilting magnitude $V_t = 3 \times 10^{11}\ s^{-2}$ (cyan).

filaments, thereby rendering streamwise vortex tubes in an irregular and asymmetric manner.

4.1. Instantaneous flowfields

To further analyze the vortical structures and mixing process, the instantaneous flowfields are examined. Fig. 6 shows snapshots of the flowfields depicted by the jet-fluid concentration C and the vorticity magnitude $|\omega|$ on the $y = 0$ plane, within the range $-5 \le x/d \le 10$ and $-1 \le z/d \le 8$. The main difference among those cases appears in the behaviors of windward rolling vortices. In Case 2, these vortices break up shortly after the jet exits the injection orifice and interacts with the cavity flow. Significantly larger structures than those in the baseline case are observed, along with lower characteristic frequencies. Conversely, in Case 4 with a wider cavity, windward rolling vortices form earlier and feature larger volume compared to the baseline case. The interaction between the jet and cavity flow becomes less intense compared with that in Case 2. The initial development of the jet in a deeper cavity (i.e., Cases 2 and 4) are that the jet initially travels vertically before significant bending occurs near $x/d = 1$. The jet then loses its coherent structure and begins to mix with the crossflow fluid. Meanwhile, the cavity flow disrupts the windward rolling vortices on the jet surface, creating fine vortex tubes that enhance mixing in the near field. The snapshots of the vorticity magnitude $|\omega|$ in Fig. 6b further illustrates this evolution, highlighting the impact of the cavity on the jet flow dynamics. The most pronounced influence of the cavity occurs in Case 2, when the injection orifice is located near the reattachment point of the front recirculating flow within the cavity. These observations provide critical insights for optimizing cavity design to modulate jet behaviors.

To identify the characteristic frequencies f of the windward rolling vortices and cavity flow, instantaneous data recorded at probes are analyzed. Fig. 7 shows the power spectral densities (PSD) of the velocity fluctuations u' and w' on the $y = 0$ plane (a) at the jet centerline $s/d = 2$ from the injection orifice along the jet centerline, and (b) in the front part of the cavity at $x/d = -1/2$, $z/h = -1/2$. The spanwise velocity fluctuation v' is omitted due to its small magnitude. The velocity fluctuations at $s/d = 2$ from the injection orifice along the jet centerline reflects the rotating motion of the windward rolling vortices. Fig. 7a shows that the baseline case and Case 3 have the highest dominant frequency, while the dominant frequency decreases for Case 1, 4 and 2. Fig 7b shows that in the front part of the cavity, the dominant frequencies are the same as those at the jet centerline $s/d = 2$. This implies that importance of cavity flow modulation in the initial formation of jet windward rolling vortices, which subsequently convect downstream and become the main flow structure.

Table 2 summarizes the dominant frequencies for the baseline case and Cases 1-4. The corresponding Strouhal numbers $St = fd/U_j$, are defined by the jet centerline velocity U_j and the jet diameter d. Note that the frequencies with a deep cavity (Cases 2 and 4) are notably lower than the value of 107 kHz in the baseline case, while the frequency in Case 1 with a narrow and shallow cavity is slightly lower. This finding implies that compared to cavity radius, cavity depth has a more profound influence on the characteristic frequencies of shear layer vortices. For a given cavity radius, an increase in cavity depth from $h/d = 0.5$ in Case 1 to 1.0 in Case 2 leads to a substantial decrease in the characteristic frequency. Conversely, for a given cavity depth, the characteristic frequency increases as the cavity radius increases from $r/d = 1.5$ in Case 2 to 2.5 in Case 4. In Case 3, with a relatively wider and shallower cavity ($r/d = 2.5$ and of $h/d = 0.5$), the characteristic frequency remains consistent with the baseline value. These observations underscore the significance of the aspect ratio of the cavity in modulating the dynamical behaviors of the JICF system and suggest a stronger influence from cavity depth.

Given the fact that a deeper cavity exerts a stronger influence on the enhancement of near-field jet mixing, further analysis is conducted for Cases 2 and 4. The dominant frequencies of these two cases are 50 kHz and 66 kHz, respectively. The corresponding periods for generating windward rolling vortices are $\tau_1 = 2.0\ \times 10^{-5}s$ and $\tau_2 = 1.5\ \times 10^{-5}s$, respectively. Fig. 8 shows close-up snapshots of the jet evolution within the cavities, captured at intervals of $0.5\ \times\ 10^{-5}s$. These snapshots are colored by the jet-fluid concentration and overlaid by two-dimensional velocity vectors on the $y = 0$ plane. Note that both cavities in Cases 2 and 4, with the length-to-depth ratio of 3 and 5, respectively, are classified as open-type cavities according to Ref. [34]; each cavity features a large recirculation zone with a shear layer across its span. The introduction of a transverse jet leads to the formation of a smaller recirculation zone ahead of the jet, as shown in Fig. 8. Compared to Case 4, the narrower cavity in Case 2 has a jet-induced recirculation zone that

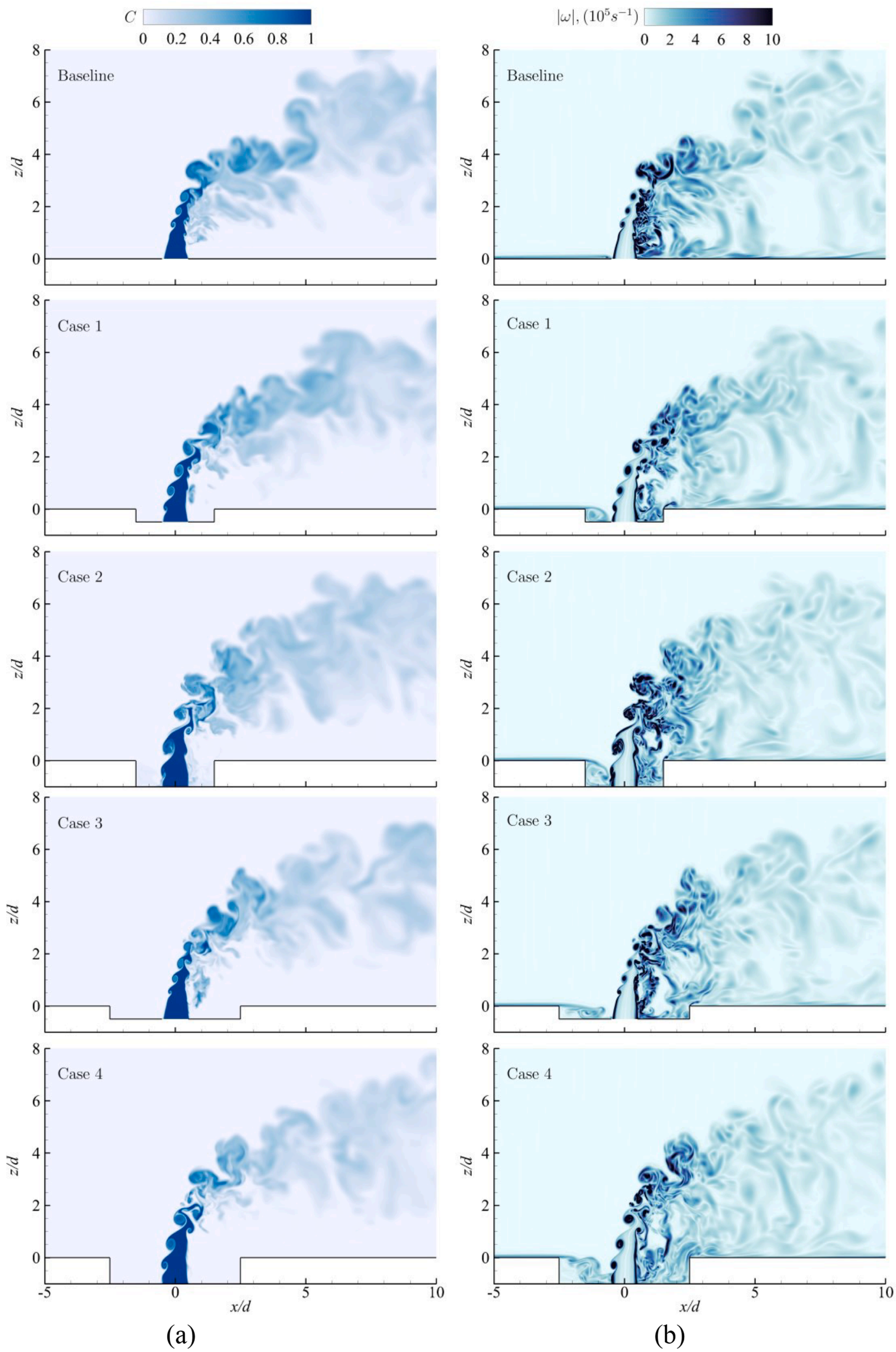

Fig. 6. Snapshots of (a) jet-fluid concentration C, and (b) vorticity magnitude $|\omega|$ on the $y = 0$ plane.

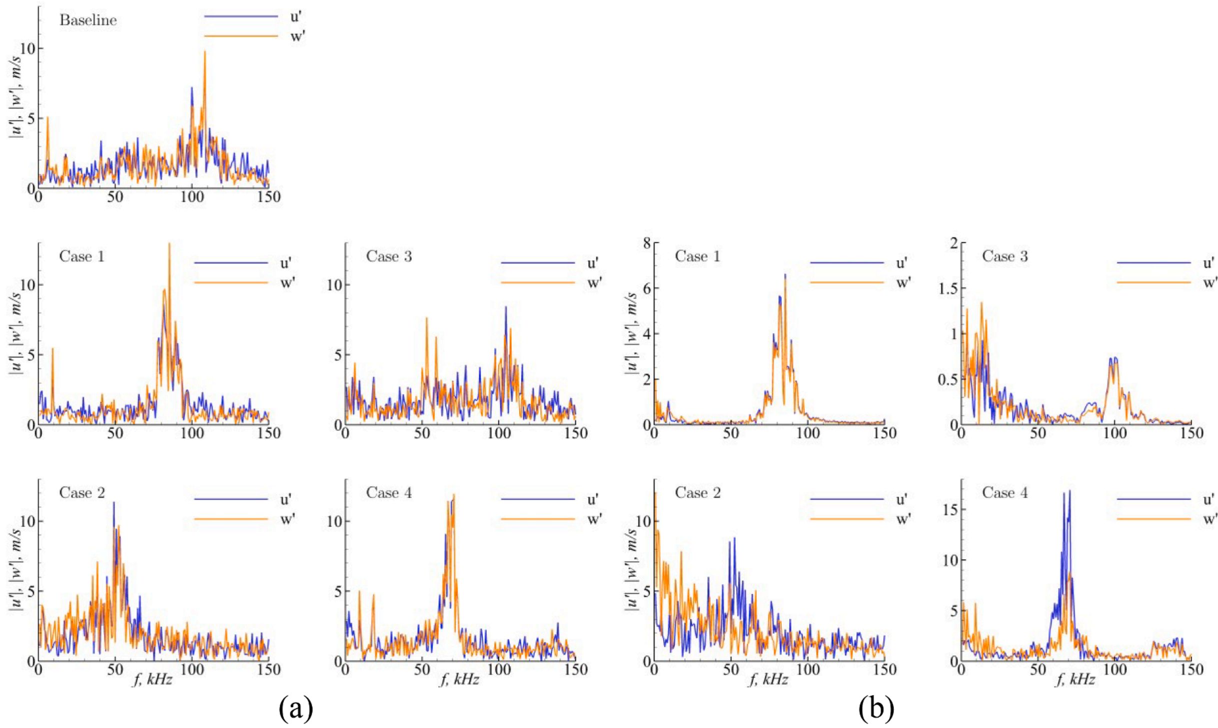

Fig. 7. Power spectral densities of velocity fluctuations u' and w' on the $y = 0$ plane (a) at $s/d = 2$ from the injection orifice along the jet centerline, (b) in the front part of the cavity at $x/d = -1/2$, $z/h = -1/2$.

Table 2
Characteristic frequencies and Strouhal numbers of windward rolling vortices.

Cases	Baseline	1	2	3	4
f (kHz)	107	85	50	107	66
St	0.8493	0.6747	0.3969	0.8493	0.5239

remains closer to the cavity wall. Such confined environment intensifies the interaction between the recirculation zone and shear layer vortices, thereby altering the shapes and spacing of the rolling vortices on the jet. Since the gap between adjacent vortices provides a region favorable for the entrainment of crossflow by the jet fluid, these variations in the vortical structures affect the efficiency of jet mixing.

4.2. Time-averaged flowfields

The flow structure is further examined by time-averaging the velocity field. Fig. 9 shows the near-field streamlines that originate from the locations $x = -r - 0.5d$, $-r \leq y \leq r$, $z = 0.05d$ upstream of the cavity. Colored by the velocity magnitude, these streamlines delineate the recirculating flow in the front part of the cavity, the skewed mixing layer, the helical flow surrounding the jet, and the entrainment of the crossflow by the jet. The leeward side of the cavity wall behaves like a forward-facing step and facilitates an upward motion of the cavity flow. In the baseline case, streamlines released at $0.05d$ above the injection orifice deflect around the jet toward the leeward side as they approach the jet. Subsequently, some streamlines separate in the low-pressure region directly behind the jet and are carried away by the upward-moving jet fluid, while others continue into the wake region. This upward movement is indicative of the early formation of the CVP. In scenarios involving a cavity, streamlines released at $h + 0.05d$ above the injection orifice exhibit different behaviors as they approach the jet; some immediately separate ahead of the jet and are entrained into the recirculation zone around the jet inside the cavity. As these streamlines move into the leeward side of the jet, their upward motions are strongly influenced by the cavity wall. In Case 1, with a narrow and shallow cavity, the streamlines exhibit behaviors similar to their counterparts in the baseline, though the upward motion is less pronounced. The flow recirculation in the front part of the cavity and the helical motion surrounding the jet are clearly observed. In Case 2, with a narrow and deep cavity, a significant increase in the upward motion occurs, suggesting enhanced crossflow entrainment in near field as the cavity deepens. The helical motion of the cavity flow is also shown but with less steadiness and regularity compared to Case 1.

In Case 4, with a wide and deep cavity, the upward motion is less intense than that in Case 2. Also, there is no streamlines in the wake region. This suggests that a wider cavity may reduce crossflow entrainment. The recirculating and helical motions of the cavity flow become less regular, similar to the situation in Case 2. In Case 3, with a wide and shallow cavity, the upward motion becomes minimal. All the streamlines remain in the wake region, indicating a decrease in crossflow entrainment and a reduction in near-field mixing.

The effects of a cavity on jet mixing are examined. Fig. 10a shows the distributions of the time-averaged jet-fluid concentration $\langle C \rangle$ on the $y = 0$ plane. Significant differences are observed between the windward and leeward sides of the jet. Specifically, the mixed fluids, for example in the range of $0.3 \leq \langle C \rangle \leq 0.7$, are primarily present on the windward side of the jet in Cases 2 and 4. This contrasts the situation in the baseline case, where, mixing is relatively evenly distributed on both sides of the jet, with a slight bias toward the leeward side. The relative importance of windward rolling-vortex induced mixing versus leeward CVP-entrainment induced mixing is examined. Cases 1 and 3 exhibit flow structures similar to the baseline case, due to the shallow cavity geometry. A maximum mixing enhancement, especially in the near field, is observed in Case 2. This phenomenon is also supported by the discussions in Figs. 3, 4 and 6.

The variances of flow variables provide insights into regions that are most significant for various activities. Fig. 10b shows the distributions of jet-fluid concentration variance $\langle C'^2 \rangle$ on the $y = 0$ plane. Regions with significant concentration variance, specifically where $\langle C'^2 \rangle > 0.03$,

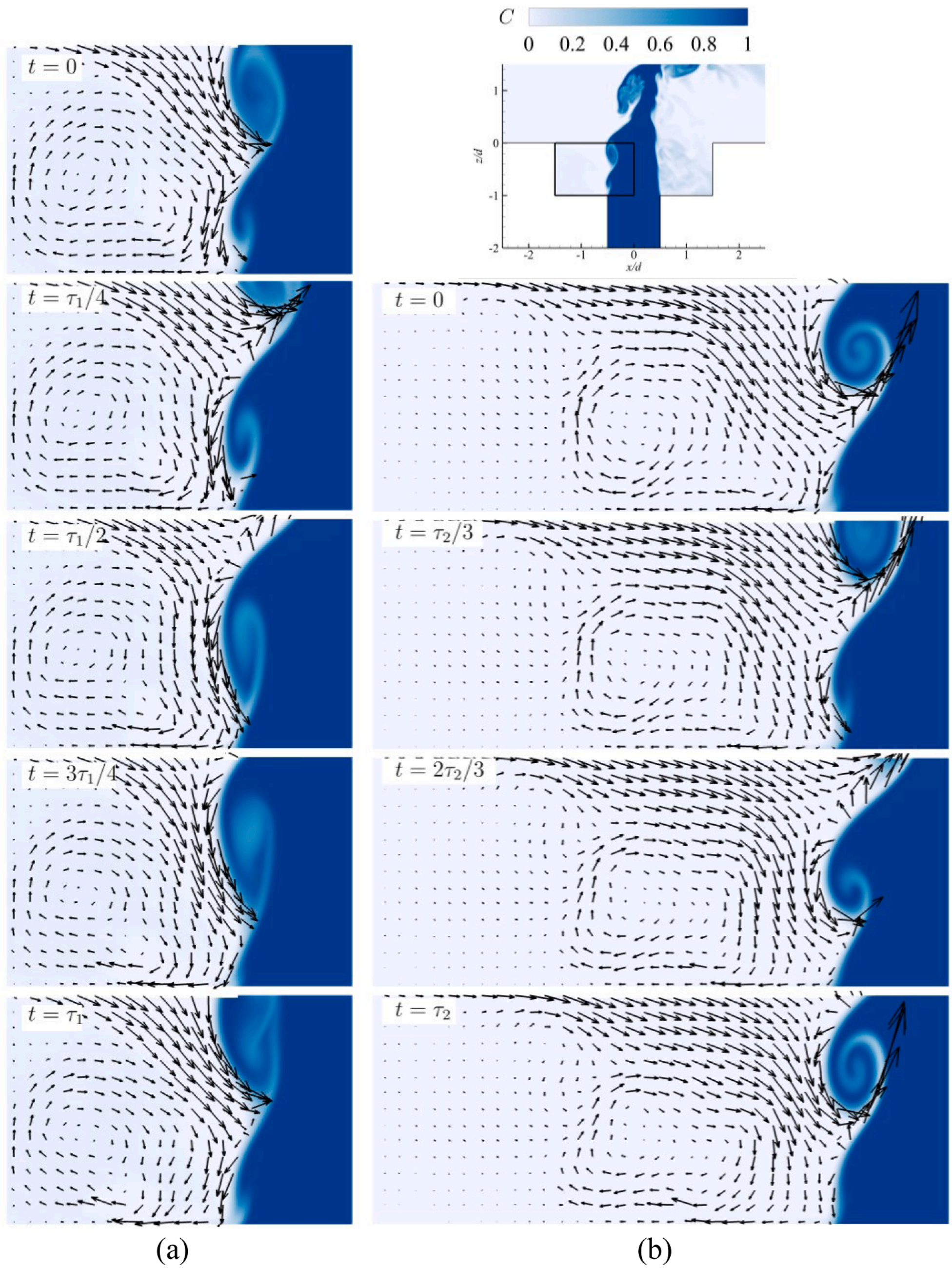

Fig. 8. Close-up snapshots of jet-fluid concentration C overlaid by velocity vectors on the $y=0$ plane, where the time periods are (a) $\tau_1 = 2.0 \times 10^{-5}$s for Cases 2, and (b) $\tau_2 = 1.5 \times 10^{-5}s$ for Case 4.

show accelerated shrinking downstream, suggesting enhanced mixing in Cases 2 and 4 compared to the baseline case. Similarly, Cases 1 and 3, with a shallow cavity ($h/d = 0.5$), exhibit a similar trend but with less significant concentration variances on the windward and leeward sides of the jet compared to Cases 2 and 4 with $h/d = 1$. These observations further substantiate the critical role of cavity depth in influencing the jet-cavity flow interaction.

Fig. 11a shows the distributions of time-averaged vorticity magnitude $|\langle\omega\rangle|$ on the $y=0$ plane. Coherent vortical structures exist in the upstream region of the cavity in all four cases. High vorticity levels, e.g., $|\langle\omega\rangle| \geq 5 \times 10^5 s^{-1}$, mainly exists within the cavity in Case 2, while they extend to a higher location in the baseline case. The spreading of the windward and leeward vorticities, e.g., $|\langle\omega\rangle| \geq 1.5 \times 10^5 s^{-1}$, is relatively limited in Cases 2 and 4 compared to the baseline case, suggesting enhanced mixing in those cases due to the cavity flow-jet interaction in the near field. A deeper cavity results in larger and stronger vortices in the cavity, which interact more intensely with the jet. Overall, the cavity depth plays a more important role than its radius. The maximum effect occurs when the jet is issued near the reattachment point of the upstream recirculating flow in a cavity with a relatively small radius.

Fig. 11b shows the time-averaged distribution of normalized resolved turbulent kinetic energy (TKE), $\left(u'^2 + v'^2 + w'^2\right)/U_j^2$, on the $y=0$ plane. The sgs TKE is about 1 % of the resolved-scale TKE, due to the small volume of the numerical grid. Thus, only the resolved TKE is shown. Strong turbulence intensity is observed around the jet. The cavity diffuses turbulent motions, and consequently enhances the jet mixing with the crossflow. This effect becomes most pronounced in Case 2 with a narrow and deep cavity.

Fig. 12 shows the distributions of (a) time-averaged jet-fluid concentration $\langle C\rangle$, (b) jet-fluid concentration variance $\langle C'^2\rangle$, and (c) time-

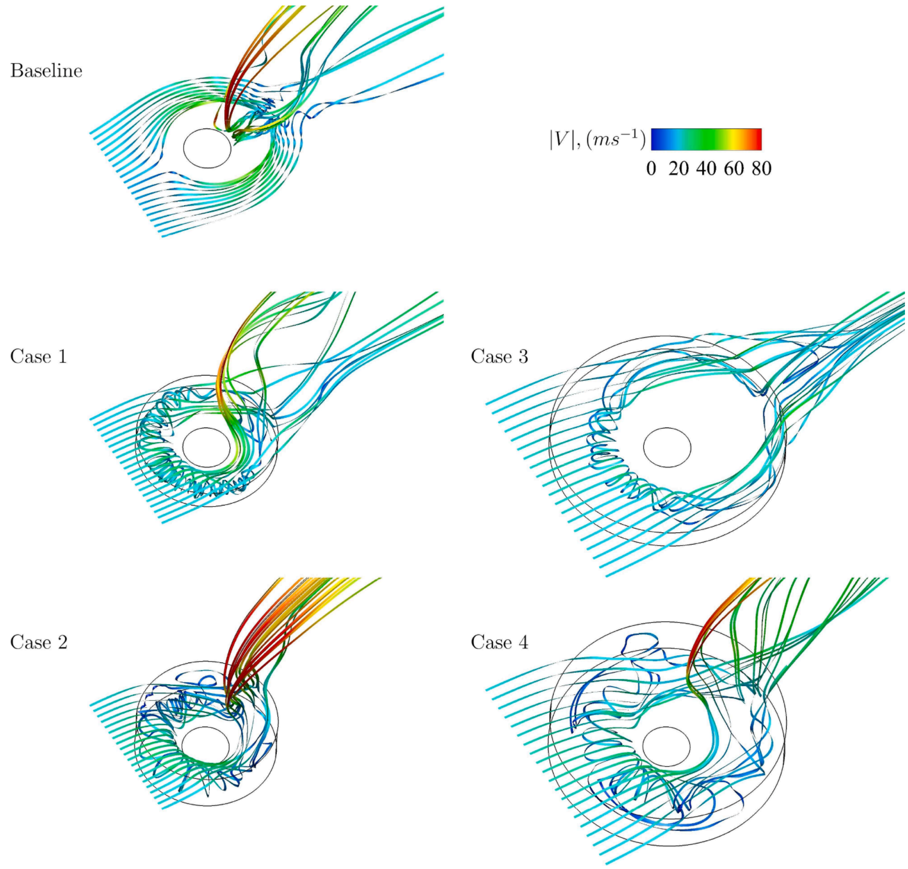

Fig. 9. Streamlines of time-averaged flowfields within and near the cavity, colored by the velocity magnitude. In Cases 1-4, streamlines originate from the locations of $x = -r - 0.5d$, $-r \le y \le r$, and $z = 0.05d$. In the baseline case, the origins of streamlines are consistent with those in Cases 1 and 2.

averaged TKE on the cross section at $x/d = 2$. The asymmetric structures of the CVPs in Cases 1 and 4 may be attributed to the bifurcation phenomenon of JICF with a velocity ratio $R = 4$ and the influence of the cavity at high Reynolds numbers. In the baseline case, the time-averaged jet-fluid concentration $\langle C \rangle$ shows a kidney shape of the CVP. The TKE and jet-fluid concentration variance $\langle C'^2 \rangle$ suggests that turbulent mixing mainly takes place in the windward side of the jet in the near field. In the Case 2, the jet-fluid concentration $\langle C \rangle$ also shows a kidney shape of the CVP, while the TKE and jet-fluid concentration variance $\langle C'^2 \rangle$ reveal that turbulent mixing extends more toward the leeward side of the CVP and is distributed more evenly in the outer region of the CVP. The unsteady helical motion of the cavity flow on the lateral sides of the jet forms a skewed mixing region and subsequently influences the initial development of the CVP. With the convection of vortical structures from the windward side to the lateral and leeward sides of the nascent CVP, the TKE and jet-fluid concentration variance $\langle C'^2 \rangle$ increase toward the leeward side of the kidney-shaped CVP in the near field. In addition, the leeward side of the cavity behaves similar to a forward-facing step and provides an upward motion of the cavity flow. The strong local flow motion enhances turbulent mixing and reinforces the strength of the CVP.

Turbulent stresses and jet-fluid concentration fluxes provide insights and correlations with the various activities in the flowfield. Fig. 13 shows the distribution of time-averaged turbulent stress $\langle u'w' \rangle / U_\infty U_j$ on the $y = 0$ plane. Fig. 14 shows the distributions of time-averaged turbulent jet-fluid concentration fluxes, $\langle u'C' \rangle / U_\infty$ and $\langle w'C' \rangle / U_j$, on the $y = 0$ plane. Since the intensity of spanwise velocity fluctuation $\langle v'v' \rangle$ is small for most cases on the symmetric plane $y = 0$, resolved turbulent stresses $\langle u'v' \rangle$ and $\langle v'w' \rangle$ and resolved turbulent jet-fluid concentration flux $\langle v'C' \rangle$ are not presented here. Detailed interpretation of turbulence correlations of JICF was given by Su and Mungal [15] and Yuan et al. [18]. The correlations are attributed to the windward and leeward rolling vortices, large scale flow structures, and jet-fluid concentration decay [15,18]. A simple interpretation is given here. On the windward side, when the crossflow is entrained by the rolling vortices of the jet, the crossflow fluid carries excess u velocity ($u' > 0$), along with lower w velocity ($w' < 0$). Therefore, the turbulent stress $\langle u'w' \rangle$ is negative on the windward side. On the leeward side, when the crossflow is entrained by the jet, $u' < 0$ and $w' < 0$, thus $\langle u'w' \rangle$ is positive. The turbulent jet-fluid concentration flux $\langle u'C' \rangle$ exhibits a similar behavior. The jet-fluid concentration C decreases ($C' < 0$) during the entrainment of the crossflow into the rolling vortices of the jet. The process increases both the w-velocity ($w' > 0$) and the jet-fluid concentration ($C' > 0$), thereby leading to positive $\langle w'C' \rangle$ near the windward side of the injection orifice. On the other hand, the negative w-velocity fluctuation ($w' < 0$) in the lower part of the jet on the leeward side renders negative $\langle w'C' \rangle$.

Fig. 13 shows the distributions of time-averaged turbulent stress $\langle u'w' \rangle / U_\infty U_j$ on the $y = 0$ plane. Negative values prevail on the windward side, especially Cases 2 and 4, due to the presence of rolling vortices. Such regions of negative turbulent stress start much earlier and closer to the injection orifice for Cases 2 and 4, compared with the baseline case. The cavity facilitates the formation of windward rolling vortices. Positive turbulent stress takes place on the leeward side of the jet. It has higher values in Cases 2 and 3, a situation attributed to the strong turbulent fluctuations. The windward rolling vortices and turbulence structures also contribute to the stronger entrainment on the leeward side of the jet. The earlier breakdown of the coherent structures in Case 2 tends to shorten the region of positive turbulent stress. In Fig. 14, the turbulent jet-fluid concentration flux $\langle u'C' \rangle$ exhibits a trend similar to the turbulent stress $\langle u'w' \rangle$. For turbulent jet-fluid

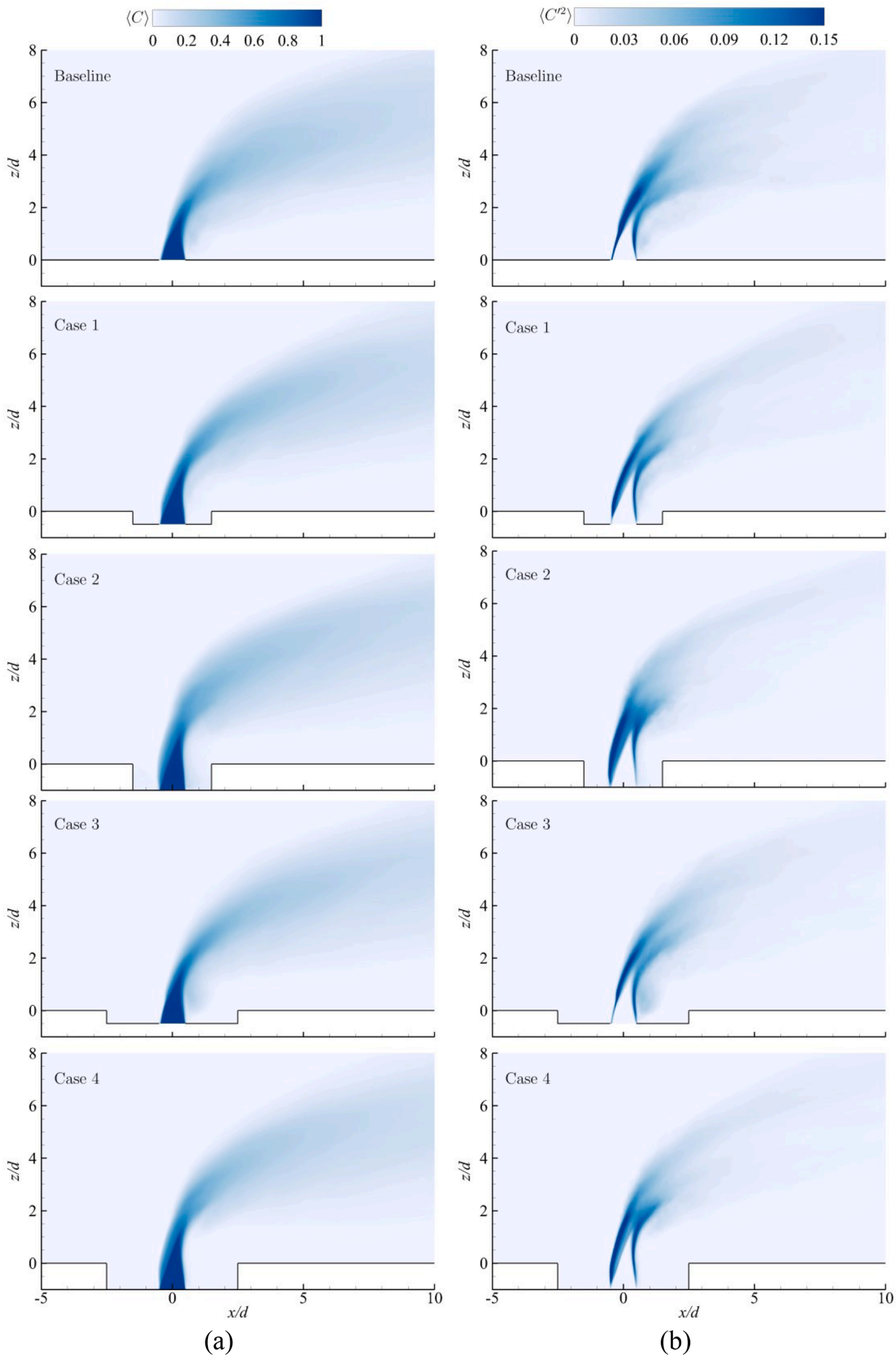

Fig. 10. Distributions of (a) time-averaged jet-fluid concentration $\langle C \rangle$, and (b) jet-fluid concentration variance $\langle C'^2 \rangle$ on $y = 0$ plane.

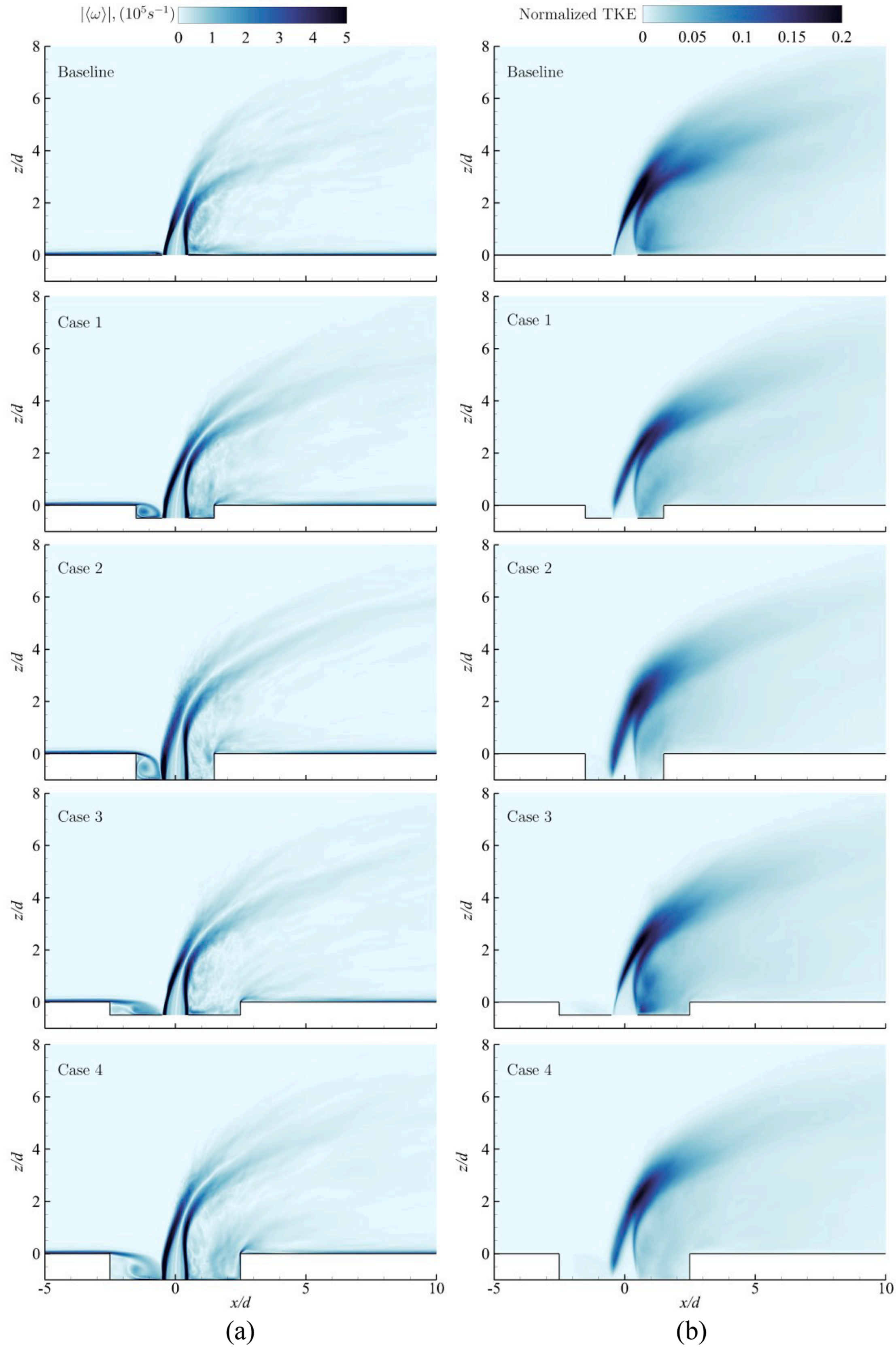

Fig. 11. Distributions of time-averaged (a) vorticity magnitude $|\langle\omega\rangle|$ and (b) normalized resolved TKE, $(u'^2 + v'^2 + w'^2)/U_j^2$, on $y = 0$ plane.

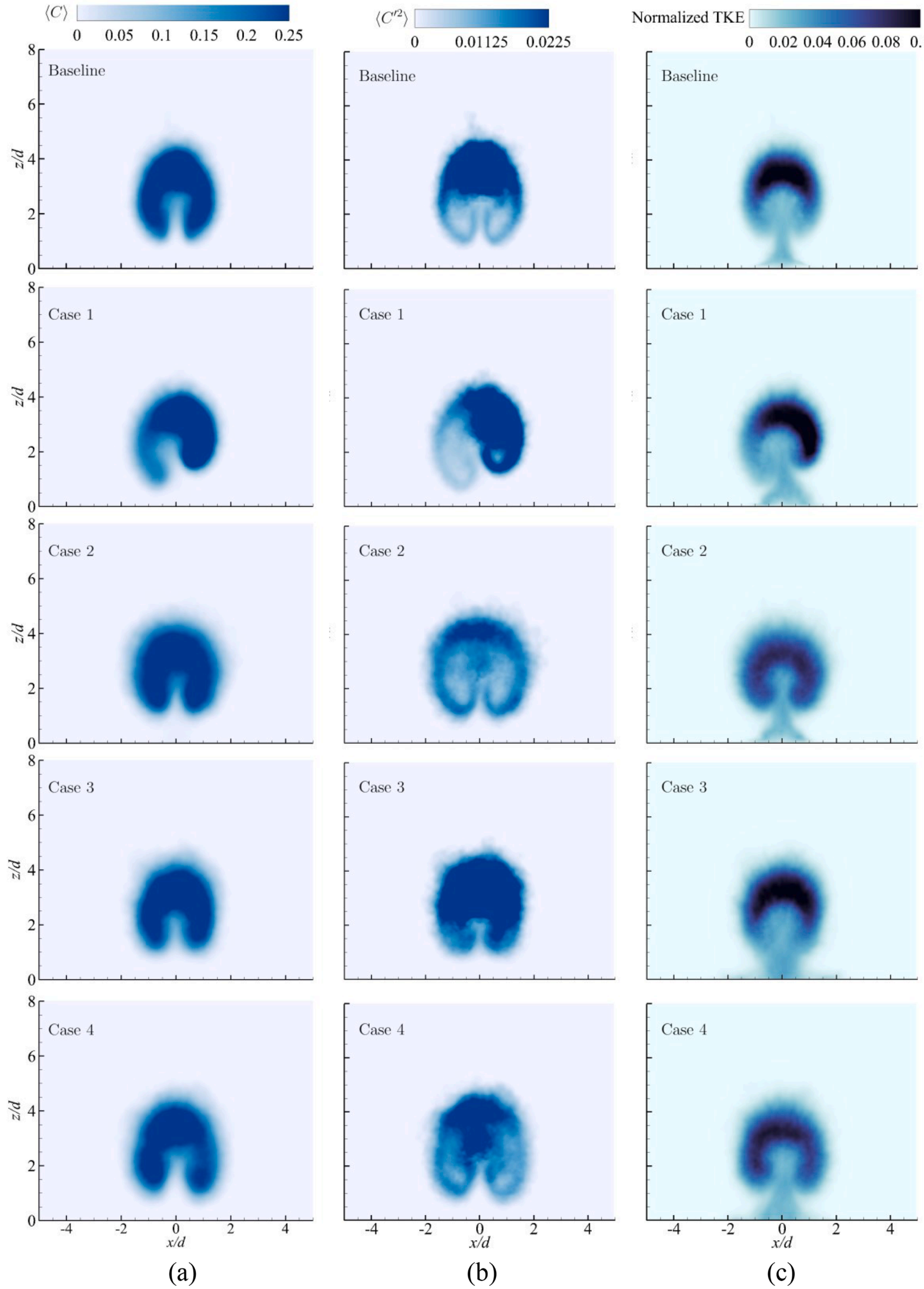

Fig. 12. Distributions of (a) time-averaged jet-fluid concentration $\langle C \rangle$, (b) jet-fluid concentration variance $\langle C'^2 \rangle$, and (c) time-averaged normalized resolved TKE on cross section at $x/d = 2$.

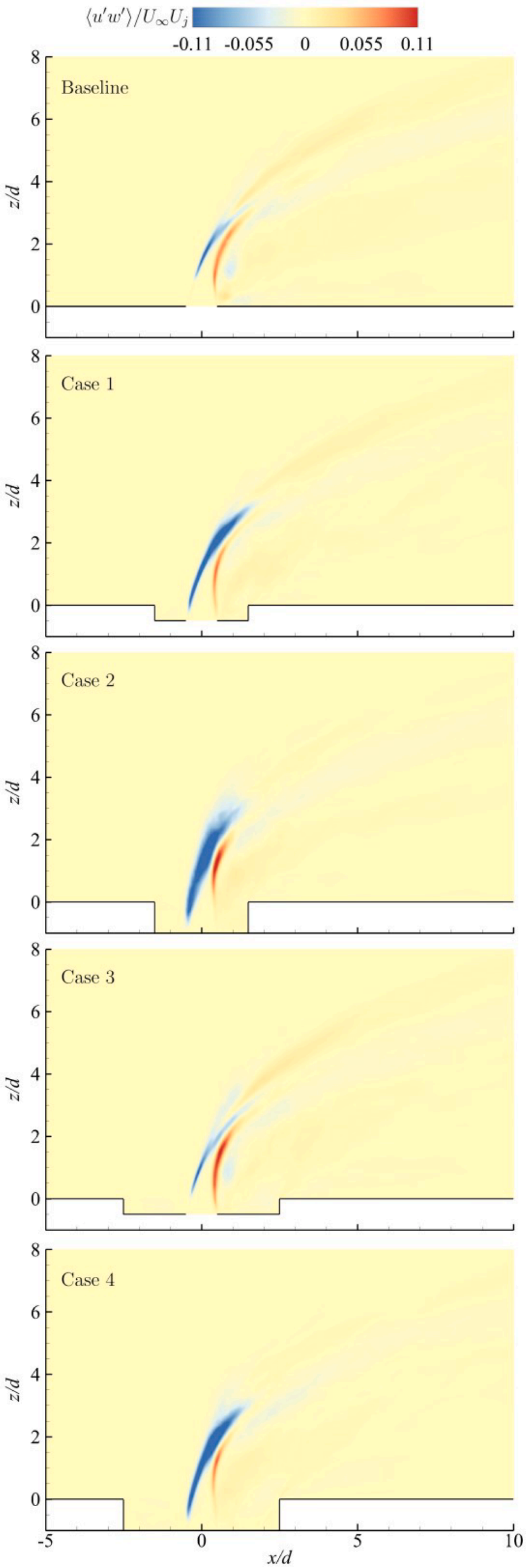

Fig. 13. Distributions of time-averaged turbulent stress $\langle u'w' \rangle / U_\infty U_j$ on $y = 0$ plane.

concentration flux $\langle w'C' \rangle$, compared to the baseline case, significant strengthening of the positive-value regions on both the windward and leeward sides of the jet is observed in Case 2, due to the formation of stronger rolling vortices. The stronger entrainment due to the windward-side vortical structures and the leeward-side cavity flow also contribute to higher $\langle w'C' \rangle$ on the leeward side by carrying more crossflow into the leeward side of the jet.

5. Mixing characteristics

The spatial mixing deficiency (SMD), the temporal mixing deficiency (TMD), and the maximum jet-fluid concentration are investigated to assess the mixing properties of the JICF system with a cavity. The SMD measures the spatial heterogeneity of the time-averaged flow quantity, while the TMD represents a spatial average of the temporal heterogeneity at various points across a plane. Both indices are calculated based on n snapshots of jet-fluid concentration over the plane of interest. They are calculated as follows.

$$\mathrm{SMD} = \frac{RMS_{plane}(\langle C_i \rangle)}{Avg_{plane}(\langle C_i \rangle)} \tag{21}$$

$$\mathrm{TMD} = Avg_{plane}\left(\frac{RMS(C_i)}{\langle C_i \rangle}\right), \text{for } \langle C_i \rangle > 0.01 \tag{22}$$

where

$$RMS_{plane}(\langle C_i \rangle) = \sqrt{\frac{1}{A}\int \left[\langle C_i \rangle - Avg_{plane}(\langle C_i \rangle)\right]^2 dA} \tag{23}$$

$$Avg_{plane}(\langle C_i \rangle) = \frac{1}{A}\int \langle C_i \rangle dA \tag{24}$$

$$\langle C_i \rangle = \frac{1}{n}\sum_{k=1}^{n} C_{i,k} \tag{25}$$

$$RMS(C_i) = \sqrt{\frac{1}{n-1}\sum_{k=1}^{n}\left(C_{i,k} - \langle C_i \rangle\right)^2} \tag{26}$$

and $\langle C_i \rangle$ is the jet-fluid concentration at point i, A the area of the plane. When computing TMD over a plane, the jet-fluid concentration may approach or even reach zero in certain regions, rendering the calculation of TMD problematic. Denev et al. [50] suggested using a jet-fluid concentration threshold $\langle C \rangle$ for the TMD calculation. In the current study, a threshold value of $\langle C \rangle = 0.01$ is applied. The SMD and TMD are calculated across several cross-sectional planes along the streamwise direction, extending up to $x/d = 20$.

Fig. 15a shows the streamwise distributions of SMD in the range of $0 < x/d < 20$. Two observations are noted. First, the cavity enhances mixing in the near field, but this effect diminishes in the far field as the dominant mixing mechanism transitions to counter-rotating vortex pairing, rather than Kelvin-Helmholtz instability. Second, the cases with deeper cavities (Cases 2 and 4) exhibit the best mixing enhancement, although the impact is modest.

Fig. 15b shows the distributions of TMD in the range of $0 < x/d < 20$. The TMD first decreases considerably in $0 < x/d < 4$, then fluctuates slightly in $4 < x/d < 12$, and finally levels off further downstream. The high TMD values in Cases 2 and 4 in the upstream region manifest the interaction between the jet and cavity flow, contributing to the high temporal variation near $x = 0$. The elevated TMD in Case 3 indicates the importance of cavity geometry in reducing the temporal variation of mixedness for the JICF system in practical applications.

Fig. 15c shows the distributions of time-averaged maximum jet-fluid concentration $\langle C \rangle$ in the logarithmic scale over the range of $0 < x/d < 20$. The maximum $\langle C \rangle$ of each case fall around a straight line,

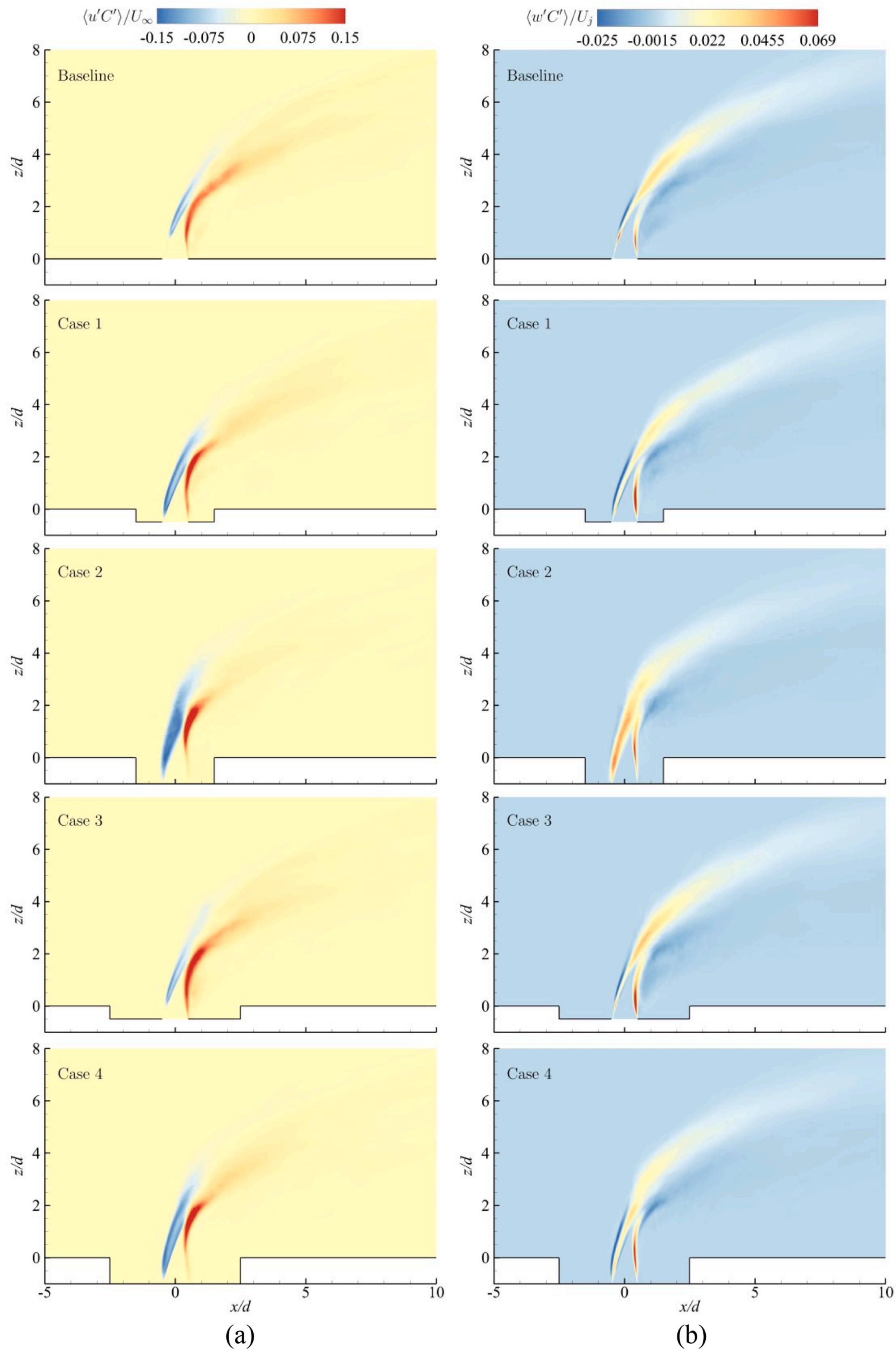

Fig. 14. Distributions of time-averaged turbulent jet-fluid concentration fluxes (a) $\langle u'C' \rangle / U_\infty$ and (b) $\langle w'C' \rangle / U_j$ on $y = 0$ plane.

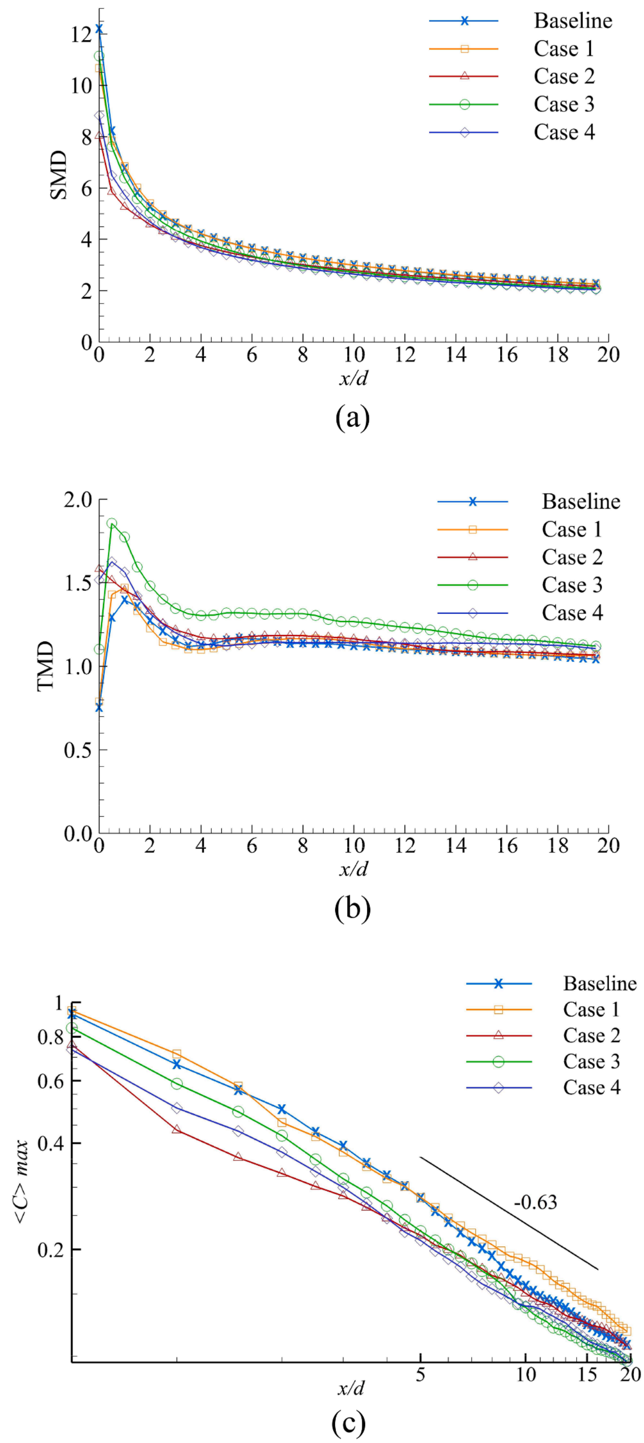

Fig. 15. Spatial evolutions of (a) SMD, (b) TMD, and (c) maximum jet-fluid concentration $\langle C\rangle$.

suggesting a power-law scaling after the initial development of the jet in the near field. The powers of the baseline case and Cases 1–4 are -0.7274, -0.6114, -0.5189, -0.6692, and -0.6014, respectively. The averaged power of -0.63 is also shown in Fig. 15c. The baseline case has the highest $\langle C\rangle$ decay rate, while Case 2 has the lowest decay rate.

6. Conclusion

The flow dynamics and mixing characteristics of an air jet issued from a cylindrical cavity in air crossflow are numerically studied using a large-eddy-simulation technique. The cavity, concentric with the jet, is located underneath the crossflow. The cavity geometry is parameterized by its depth h and radius r. Four different cavity geometries ($r/d = 1.5,\ 2.5,$ and $h/d = 0.5,\ 1.0$) are studied. The velocities of the jet and crossflow are chosen to be 160 and 40 m/s, respectively, to mimic the flow conditions of operational gas turbine engines. The jet-to-crossflow velocity ratio is 4, and the Reynolds number of the jet is 1.39×10^4, based on its centerline velocity and diameter.

The cavity significantly impacts the initial evolution of the jet and its interaction with the crossflow. First, windward rolling vortices on the jet surface increase in size, accompanied by a reduced frequency. The situation is most pronounced in cases with a deep cavity (Cases 2 and 4). These vortices may even break down and result in small vortical tubes in the jet streamwise direction due to secondary instability, further enhancing the crossflow entrainment in the near field. Since the gaps between vortices serve as favorable regions for crossflow entrainment by the jet fluid, such variations in vortical structures improve jet mixing efficiency. Second, hanging vortices, induced by skewed mixing layers on the lateral sides of the jet and aligned with the mean convective velocity, are amplified. They promote near-field mixing by transporting the jet fluid towards the lower half of the jet plume and affect the early development of the counter-rotating vortex pair. Third, crossflow boundary-layer separation may be enhanced in the wake region, generating roller-structured wake vortices that link the near-wall region with the jet plume and affect crossflow entrainment all the way to a far downstream region. Fourth, the helical recirculating flow within the cavity encircles the jet and significantly influences its evolution. Such vortical flow motion depends strongly on the cavity radius, with more pronounced effects in cases with narrow cavities (Cases 1 and 2) due to their spatial confinement.

The calculated mixing indices show that the cavity enhances the mixing between the jet and crossflow. The effect is most pronounced in the near field but diminishes in the far field. This phenomenon can be attributed to the complex vortical structures discussed above, including shear-layer vortices on the windward and leeward sides, streamwise vortex tubes, hanging vortices on the lateral sides, and wake vortices of the jet, as well as the helical recirculating flow within the cavity. In the present study, the depth of the cavity plays a more important role than its radius in affecting the jet evolution and mixing. The maximum influence is observed when a narrow and deep cavity is implemented. These findings may serve as guidelines for optimizing cavity design to effectively modulate jet behaviors.

CRediT authorship contribution statement

Bichuan Mo: Writing – review & editing, Writing – original draft, Visualization, Software, Methodology, Investigation, Formal analysis, Data curation. **Vigor Yang:** Writing – review & editing, Supervision, Resources, Project administration, Funding acquisition, Conceptualization. **Liwei Zhang:** Writing – review & editing, Validation, Supervision, Software, Methodology, Investigation, Funding acquisition, Formal analysis.

Declaration of competing interest

The authors declare that they have no known competing financial interests or personal relationships that could have appeared to influence the work reported in this paper.

Data availability

Data will be made available on request.

Acknowledgments

This study partly was sponsored by the Ralph N. Read Endowment at the Georgia Institute of Technology. The work of Liwei Zhang was supported by the Faculty Startup Fund at the University of Texas at Arlington.

References

[1] R.J. Margason, Fifty years of jet in cross flow research, in: Proceedings of the AGARD Symposium on Computational and Experimental Assessment of Jets in Crossflow, Winchester, UK, 1993, pp. 1–41. AGARD-CP-534.
[2] A.R. Karagozian, Transverse jets and their control, Prog. Energy Combust. Sci. 36 (2010) 531–553.
[3] K. Mahesh, The interaction of jets with crossflow, Annu. Rev. Fluid Mech. 45 (2013) 379–407.
[4] A.R. Karagozian, The jet in crossflow, Phys. Fluids 26 (2014) 1–47.
[5] L. Zhang, V. Yang, Flow dynamics and mixing of a transverse jet in crossflow—Part I: steady crossflow, J. Eng. Gas Turbines Power 139 (2017) 082601, https://doi.org/10.1115/1.4035808.
[6] L. Zhang, V. Yang, Flow dynamics and mixing of a transverse jet in crossflow—Part II: oscillating crossflow, J. Eng. Gas Turbines Power 139 (2017) 082602, https://doi.org/10.1115/1.4035809.
[7] T. Fric, A. Roshko, Vortical structure in the wake of a transverse jet, J. Fluid Mech. 279 (1994) 1–47.
[8] R.M. Kelso, T. Lim, A. Perry, An experimental study of round jets in cross-flow, J. Fluid Mech. 306 (1996) 111–144.
[9] S. Muppidi, K. Mahesh, Direct numerical simulation of round turbulent jets in crossflow, J. Fluid Mech. 574 (2007) 59–84.
[10] S. Bagheri, P. Schlatter, P.J. Schmid, D.S. Henningson, Global stability of a jet in crossflow, J. Fluid Mech. 624 (2009) 33–44.
[11] L. Cortelezzi, A.R. Karagozian, On the formation of the counter-rotating vortex pair in transverse jets, J. Fluid Mech. 446 (2001) 347–373.
[12] Y. Huang, V. Yang, Dynamics and stability of lean-premixed swirl-stabilized combustion, Prog. Energy Combust. Sci. 35 (2009) 293–364.
[13] D. You, Y. Huang, V. Yang, A generalized model of acoustic response of turbulent premixed flame and its application to gas-turbine combustion instability analysis, Combust. Sci. Technol. 177 (2005) 1109–1150.
[14] S. Smith, M. Mungal, Mixing, structure and scaling of the jet in crossflow, J. Fluid Mech. 357 (1998) 83–122.
[15] L. Su, M. Mungal, Simultaneous measurements of scalar and velocity field evolution in turbulent crossflowing jets, J. Fluid Mech. 513 (2004) 1–45.
[16] S. Muppidi, K. Mahesh, Direct numerical simulation of passive scalar transport in transverse jets, J. Fluid Mech. 598 (2008) 335–360.
[17] J.W. Shan, P.E. Dimotakis, Reynolds-number effects and anisotropy in transverse-jet mixing, J. Fluid Mech. 566 (2006) 47–96.
[18] L.L. Yuan, R.L. Street, J.H. Ferziger, Large-eddy simulations of a round jet in crossflow, J. Fluid Mech. 379 (1999) 71–104.
[19] L.L. Yuan, R.L. Street, Trajectory and entrainment of a round jet in crossflow, Phys. Fluids 10 (1998) 2323–2335.
[20] S. Muppidi, K. Mahesh, Study of trajectories of jets in crossflow using direct numerical simulations, J. Fluid Mech. 530 (2005) 81–100.
[21] S. Megerian, J. Davitian, L. de B Alves, A. Karagozian, Transverse-jet shear-layer instabilities. Part 1. Experimental studies, J. Fluid Mech. 593 (2007) 93.
[22] P.S. Iyer, K. Mahesh, A numerical study of shear layer characteristics of low-speed transverse jets, J. Fluid Mech. 790 (2016) 275–307.
[23] M.A. Regan, K. Mahesh, Global linear stability analysis of jets in cross-flow, J. Fluid Mech. 828 (2017) 812–836.
[24] M.A. Regan, K. Mahesh, Adjoint sensitivity and optimal perturbations of the low-speed jet in cross-flow, J. Fluid Mech. 877 (2019) 330–372.
[25] T. Shoji, E.W. Harris, A. Besnard, S.G. Schein, A.R. Karagozian, On the origins of transverse jet shear layer instability transition, J. Fluid Mech. 890 (2020) A7.
[26] B.A. Haven, M. Kurosaka, Kidney and anti-kidney vortices in crossflow jets, J. Fluid Mech. 352 (1997) 27–64.
[27] T. New, T. Lim, S. Luo, Elliptic jets in cross-flow, J. Fluid Mech. 494 (2003) 119–140.
[28] B. Wegner, Y. Huai, A. Sadiki, Comparative study of turbulent mixing in jet in cross-flow configurations using LES, Int. J. Heat Fluid Flow 25 (2004) 767–775.
[29] J.M. Seiner, S. Dash, D. Kenzakowski, Historical survey on enhanced mixing in scramjet engines, J. Propul. Power 17 (2001) 1273–1286.
[30] E.W. Harris, T. Shoji, A. Besnard, S.G. Schein, R.T. M'Closkey, L. Cortelezzi, A. R. Karagozian, Effects of controlled vortex generation and interactions in transverse jets, Phys. Rev. Fluids 7 (2022) 013902.
[31] T. Lim, T. New, S. Luo, On the development of large-scale structures of a jet normal to a cross flow, Phys. Fluids 13 (2001) 770–775.
[32] E.W. Harris, A. Besnard, A. Karagozian, Effect of tabs on transverse jet instabilities, structure, vorticity dynamics and mixing, J. Fluid Mech. 918 (2021) A8.
[33] N. Morse, K. Mahesh, Effect of tabs on the shear layer dynamics of a jet in cross-flow, J. Fluid Mech. 958 (2023) A6.
[34] S.D. Crook, T.C. Lau, R.M. Kelso, Three-dimensional flow within shallow, narrow cavities, J. Fluid Mech. 735 (2013) 587–612.
[35] C.W. Rowley, T. Colonius, A.J. Basu, On self-sustained oscillations in two-dimensional compressible flow over rectangular cavities, J. Fluid Mech. 455 (2002) 315–346.
[36] L. Larchevêque, P. Sagaut, T.H. Lê, P. Comte, Large-eddy simulation of a compressible flow in a three-dimensional open cavity at high Reynolds number, J. Fluid Mech. 516 (2004) 265–301.
[37] L. Larchevêque, P. Sagaut, O. Labbé, Large-eddy simulation of a subsonic cavity flow including asymmetric three-dimensional effects, J. Fluid Mech. 577 (2007) 105–126.
[38] L. Larchevêque, P. Sagaut, I. Mary, O. Labbé, P. Comte, Large-eddy simulation of a compressible flow past a deep cavity, Phys. Fluids 15 (2003) 193–210.
[39] H. Le, P. Moin, J. Kim, Direct numerical simulation of turbulent flow over a backward-facing step, J. Fluid Mech. 330 (1997) 349–374.
[40] S. Wang, S.Y. Hsieh, V. Yang, Unsteady flow evolution in swirl injector with radial entry. I. Stationary conditions, Phys. Fluids 17 (2005) 045106.
[41] S. Wang, V. Yang, G. Hsiao, S.Y. Hsieh, H.C. Mongia, Large-eddy simulations of gas-turbine swirl injector flow dynamics, J. Fluid Mech. 583 (2007) 99–122.
[42] G. Erlebacher, M.Y. Hussaini, C.G. Speziale, T.A. Zang, Toward the large-eddy simulation of compressible turbulent flows, J. Fluid Mech. 238 (1992) 155–185.
[43] A. Yoshizawa, Statistical theory for compressible turbulent shear flows, with the application to subgrid modeling, Phys. Fluids 29 (1986) 2152–2164.
[44] P. Moin, J. Kim, Numerical investigation of turbulent channel flow, J. Fluid Mech. 118 (1982) 341–377.
[45] J. Eggels, F. Unger, M. Weiss, J. Westerweel, R. Adrian, R. Friedrich, F. Nieuwstadt, Fully developed turbulent pipe flow: a comparison between direct numerical simulation and experiment, J. Fluid Mech. 268 (1994) 175–210.
[46] J. Jeong, F. Hussain, On the identification of a vortex, J. Fluid Mech. 285 (1995) 69–94.
[47] A. Ruiz, G. Lacaze, J. Oefelein, Flow topologies and turbulence scales in a jet-in-cross-flow, Phys. Fluids 27 (2015) 045101.
[48] J. Lasheras, H. Choi, Three-dimensional instability of a plane free shear layer: an experimental study of the formation and evolution of streamwise vortices, J. Fluid Mech. 189 (1988) 53–86.
[49] J.Z. Wu, H.Y. Ma, M.D. Zhou, Vortical Flows, Springer, 2015.
[50] J.A. Denev, J. Fröhlich, H. Bockhorn, Large eddy simulation of a swirling transverse jet into a crossflow with investigation of scalar transport, Phys. Fluids 21 (2009) 015101.